

# Towards surface-wave tomography with 3D resolution and uncertainty

Franck Latallerie  <sup>\*</sup> <sup>1</sup>, Christophe Zaroli  <sup>2</sup>, Sophie Lambotte  <sup>2</sup>, Alessia Maggi  <sup>2</sup>, Andrew Walker  <sup>1</sup>, Paula Koelemeijer  <sup>1</sup>

<sup>1</sup>Department of Earth Sciences, University of Oxford, Oxford, United Kingdom, <sup>2</sup>Institut Terre et Environnement de Strasbourg, UMR7063, Université de Strasbourg, EOST/CNRS, 67084, Strasbourg CEDEX, France

**Author contributions:** *Conceptualization:* FL, CZ, SL, AM, AW, PK. *Methodology:* FL, CZ, SL. *Software:* FL, CZ, SL. *Data curation:* FL. *Formal Analysis:* FL. *Investigation:* FL, CZ, PK. *Writing - Original draft:* FL. *Writing - Review & Editing:* FL, CZ, SL, AM, AW, PK. *Visualization:* FL. *Supervision:* CZ, SL, AM, AW, PK. *Project administration:* AW, PK. *Funding acquisition:* AM, AW, PK.

**Abstract** Surface-wave tomography is crucial for mapping upper-mantle structure in poorly instrumented regions such as the oceans. However, data sparsity and errors lead to tomographic models with complex resolution and uncertainty, which can impede meaningful physical interpretations. Accounting for the full 3D resolution and robustly estimating model uncertainty remains challenging in surface-wave tomography. Here, we propose an approach to provide direct control over the model resolution and uncertainty and to produce these in a fully three-dimensional framework by combining the Backus-Gilbert-based SOLA method with finite-frequency theory. Using a synthetic setup, we demonstrate the reliability of our approach and illustrate the artefacts arising in surface-wave tomography due to limited resolution. We also indicate how our synthetic setup enables us to discuss the theoretical model uncertainty (arising due to assumptions in the forward theory), which is often overlooked due to the difficulty in assessing it. We show that the theoretical uncertainty components may be much larger than the measurement uncertainty, thus dominating the overall uncertainty. Our study paves the way for more robust and quantitative interpretations in surface-wave tomography.

**Non-technical summary** In the oceans, several surface features such as isolated volcanic islands or variations in the depth of the seafloor result from dynamic processes in the underlying mantle. To understand these processes, we need to image the three-dimensional structures present in the subsurface. While long-period surface waves can be used for this, the data are typically noisy and provide poor coverage of the oceans. This limits the quality of our images and therefore the interpretations that can be drawn from them. In addition, limitations of our images are difficult to quantify with current methods, which makes interpretations even more difficult. In this study, we propose an approach to produce high-quality maps of 3D structures in the upper mantle, which also gives information on the quality of the images. We present the method in a synthetic framework, which serves to demonstrate our ability to retrieve an input Earth model and enables us to estimate theoretical model uncertainties. Our approach will enable more robust interpretations of surface-wave tomography models in the future.

## 1 Introduction

Many important geological processes (e.g. melting at mid-ocean ridges, spreading, subduction and hotspot volcanism) result from dynamic processes in the upper mantle. To improve our understanding of these processes, we need to robustly image the structure of the upper mantle. In poorly instrumented regions, such as the oceans, this imaging relies heavily on surface-wave tomography. However, surface-wave data have poor spatial coverage, both laterally due to the uneven distribution of earthquakes (sources) and seismic stations (receivers), and vertically due to how surface-wave sensitivity varies with depth. Surface-wave data also contain errors due to imperfect measurement and physical theory. Poor data coverage and data errors render the

inverse problem ill-posed and lead to complex model resolution and model uncertainty (e.g. Parker, 1977; Menke, 1989; Tarantola, 2005). These explain the strong discrepancies between published tomography models (e.g. Hosseini et al., 2018; Marignier et al., 2020; De Viron et al., 2021). Over time, seismic images have become more detailed and are being used to inform research in other fields. To guarantee the usefulness of surface-wave tomographic images however, we need to account for their full 3D resolution and uncertainty (e.g. Ritsema et al., 2004; Foulger et al., 2013; Rawlinson et al., 2014). Equipped with these, we will be able to avoid interpreting non-significant anomalies (e.g. Latallerie et al., 2022), set up meaningful comparisons with theoretical predictions (e.g. Freissler et al., 2020), or include tomography models in further studies such as earthquake hazard assessments (e.g. Boaga et al., 2011;

Production Editor:  
Yen Joe Tan  
Handling Editor:  
Chiara Civiero  
Copy & Layout Editor:  
Kirsty Bayliss

Received:  
July 08, 2024  
Accepted:  
June 24, 2025  
Published:  
August 13, 2025

\*Corresponding author: franck.latallerie@earth.ox.ac.uk

Socco et al., 2012; Boaga et al., 2012).

Many approaches have been proposed to solve ill-posed inverse problems in seismology (e.g. Wiggins, 1972; Parker, 1977; Tarantola and Valette, 1982; Nolet, 1985; Scales and Snieder, 1997; Trampert, 1998; Nolet, 2008). Most take a data-misfit point of view and search for a model whose predictions are ‘close enough’ to observations. However, such approaches have difficulties in accounting directly for model resolution and uncertainty, either for computational reasons or because, in these approaches, resolution and uncertainty depend in complex ways on the parameterisation and regularisations used (Nolet et al., 1999; Barmin et al., 2001; Ritsema et al., 2004; Shapiro et al., 2005; Ritsema et al., 2007; Fichtner and Trampert, 2011; An, 2012; Fichtner and Zunino, 2019; Simmons et al., 2019; Bonadio et al., 2021). Synthetic tests, sometimes in the form of checkerboard tests, can be useful to assess resolution, but these have been shown to be potentially misleading (e.g. L  v  que et al., 1993; Rawlinson and Spakman, 2016).

Other approaches for solving ill-posed inverse problems move away from the data-misfit point of view and instead concentrate on directly optimising model resolution and uncertainty. These approaches are typically based on Backus–Gilbert theory (Backus and Gilbert, 1967, 1968, 1970). One such approach, the SOLA (Subtractive Optimally Localized Averages) formulation, was derived for helioseismology by Pijpers and Thompson (1992, 1994) before being introduced and adapted to linear body-wave tomographic inversions by Zaro  li (2016) and Zaro  li (2019). Besides body waves, the method has been successfully applied to normal-mode splitting data to constrain ratios between seismic velocities (Restelli et al., 2024) and to surface-wave dispersion data to build group-velocity maps (Ouattara et al., 2019; Amiri et al., 2023) or 2D maps of the vertically polarised shear-wave velocity  $V_{SV}$  (Latal  rie et al., 2022). Although SOLA can be applied only to linear problems, it requires no prior on the model solution, provides direct control on model resolution and uncertainty, and produces solutions free of averaging bias (Zaro  li et al., 2017).

Traditionally, surface-wave tomography studies are based on ray-theory. This infinite-frequency approximation requires a two-step procedure that can be performed in either order. One order is first to solve the inverse problem laterally (to produce 2D phase or group-velocity maps) and subsequently to solve for velocity structure with depth (to produce 1D velocity profiles) (e.g. Ekstr  m et al., 1997; Montagner, 2002; Yoshizawa and Kennett, 2004; Ekstr  m, 2011; Ouattara et al., 2019; Sere  dkina, 2019; Isse et al., 2019; Magrini et al., 2022; Greenfield et al., 2022). The other approach is to solve first for velocity structure with depth for independent source-receiver pairs (to produce 1D path-averaged velocity profiles) and subsequently for lateral variations (to produce 2D velocity maps) (e.g. Debayle and L  v  que, 1997; L  v  que et al., 1998; Debayle, 1999; Debayle and Kennett, 2000; Simons et al., 2002; Lebedev and Nolet, 2003; Priestley, 2003; Debayle and Sambridge, 2004; Maggi et al., 2006b,a; Priestley and McKenzie, 2006). This second approach was adopted by Latal  rie et al. (2022) who applied the SOLA method to the

second step (lateral inversion) to produce 2D lateral resolution and uncertainty information, in addition to their tomography model. Because the first step is a non-linear depth inversion, it could not be performed using SOLA – a purely linear method. Therefore, this study was not able to provide high-quality information about vertical resolution, a significant drawback given the complex depth sensitivity of surface-waves.

In this study, we extend the approach of Latal  rie et al. (2022) to 3D using the framework of finite-frequency theory (Snieder, 1986; Snieder and Nolet, 1987; Yomogida, 1992; Marquering et al., 1998; Dahlen and Tromp, 1999; Yoshizawa and Kennett, 2004; Zhou et al., 2004, 2005; Yoshizawa and Kennett, 2005; Zhou, 2009a,b; Ruan and Zhou, 2010; Tian et al., 2011; Zhou et al., 2006; Liu and Zhou, 2016b,a). In this framework, surface-wave dispersion data are linearly related to perturbations in the 3D upper-mantle velocity structure. This makes it possible to perform a one-step inversion and thus to obtain 3D resolution information using SOLA. Finite-frequency inversions come with higher memory costs because the sensitivity kernels are volumetric (with both a lateral and depth extent) and the whole 3D model must be stored all at once (large number of model parameters). However, with smart data selection and ever increasing computational power, this memory cost is becoming less of an issue.

Model uncertainty arises from data uncertainty (or measurement uncertainty) as well as theoretical uncertainty. Data uncertainty is often estimated by comparing the dispersion of measurements for nearby rays (e.g. Maggi et al., 2006b). However, this approach dramatically underestimates the data uncertainty and accounts poorly for systematic biases (e.g. Latal  rie et al., 2022). This is less of an issue if we are only interested in the relative uncertainty between individual data (e.g. when we weigh data contributions in a data-driven inversion). Underestimated data uncertainty and bias become problematic, however, if we want to interpret the ‘true’ magnitude of the model uncertainty. It therefore becomes important to estimate data uncertainties carefully. Additionally, we need to account for imperfections in the forward theory, which give rise to ‘theoretical uncertainty’. This theoretical uncertainty arises from a range of approximations commonly made: single-scattering, which relates to non-linearity; the forward-scattering approximation; the paraxial approximation; neglected sensitivity to other parameters; discretisation onto the tomographic grid; linear crustal correction strategy; errors in the crustal model; and errors in the earthquake source parameters. These last two contributions are not accounted for in this study. The theoretical component is often missing in model uncertainty estimates, which may partly explain why these estimates appear to be small. Importantly, both measurement uncertainty and theoretical uncertainty contribute to model uncertainty. Here, we distinguish the two contributions to the model uncertainty by using the terms ‘measurement model uncertainty’ and ‘theoretical model uncertainty’. We take advantage of the synthetic nature of this study to discuss the contribution

of both contributions.

In this study, we show that it is possible to obtain detailed 3D resolution and robust uncertainty information using surface waves with SOLA within a finite-frequency framework, thus extending the approach of [Latallerie et al. \(2022\)](#) to 3D. By working in a synthetic setup, we demonstrate the feasibility of our approach, and discuss the contribution of theoretical errors. To achieve these aims, we develop a complete workflow from dispersion measurements on the waveforms to analyses of the resulting 3D model, its resolution and uncertainty. In Section 2, we introduce the SOLA method and the forward modelling approach. In Section 3, we describe the tomography setup, including the data geometry, target resolution and generalised inverse. Subsequently, in Section 4, we discuss the data and their uncertainty in detail. In Section 5, we present our tomographic results, both qualitatively and quantitatively. Finally, in Section 6, we discuss the 3D resolution and uncertainty estimates of our model and indicate possible future directions.

## 2 Theory

We present here the main building blocks of our approach. Firstly, we briefly introduce the general forward problem. We then discuss the inverse problem, introducing the discrete linear SOLA inverse method ([Zaroli, 2016](#)) that provides control on the resolution and the propagation of uncertainty, and produces the tomographic model with full resolution and uncertainty information. Finally, we present the finite-frequency theory that allows the surface-wave inverse problem to be expressed in a linear and fully three-dimensional framework.

### 2.1 General forward theory

Let  $\mathbf{d} \in \mathcal{R}^N$  be a data vector and let  $\mathbf{m} \in \mathcal{R}^M$  be a model vector containing model parameters given a pre-defined parameterisation. Let  $\mathbf{G} \in \mathcal{M}(N \times M)$  be the sensitivity matrix (in the set of matrices of size  $N \times M$ ), describing a linear relationship between model parameters and data. We can then write the forward problem as:

$$\mathbf{d} = \mathbf{G}\mathbf{m}. \quad (1)$$

Rows of  $\mathbf{G}$  are the sensitivity kernels and  $\mathbf{G}$  thus contains all the information regarding the sensitivity of the entire dataset to all model parameters; this is what we refer to as the data geometry.

To account for data errors, we treat  $\mathbf{d}$  as a normally distributed multi-variate random variable with data covariance matrix  $\mathbf{C}_d \in \mathcal{M}(N \times N)$ . We assume uncorrelated noise, thus the data covariance matrix is diagonal and we can write  $\mathbf{C}_d = \text{diag}(\sigma_{d_i}^2), i \in [1, N]$ , where  $\sigma_{d_i}$  is the standard deviation of the error on the  $i^{\text{th}}$  datum. Throughout this study, we refer to the standard deviation as the data uncertainty. Note that under the Gaussian hypothesis both theoretical errors (due to imperfect forward theory) and measurement errors (due to imperfect measurements) can be included in

$\sigma_{d_i}^2$  (see e.g. [Tarantola, 2005](#)). As it is challenging to estimate error correlations, we assume uncorrelated errors, which we further assume to be Gaussian for mathematical simplicity. The assumption of Gaussian uncorrelated errors remains an important limitation that should motivate future work.

### 2.2 SOLA inverse method

Poor data geometry in seismic tomography makes the inverse problem ill-constrained as the sensitivity matrix  $\mathbf{G}$  is not invertible. This justifies the use of various existing methods for obtaining model solutions (see e.g. [Parker, 1977](#); [Trampert, 1998](#); [Scales and Snieder, 1997](#); [Nolet, 1985](#); [Tarantola and Valette, 1982](#); [Wiggins, 1972](#); [Nolet, 2008](#)). Most of these methods use a data-misfit approach, where a model solution is found by minimising the discrepancy between predicted data and the actual data. With SOLA, we do not use a data-misfit to drive towards a model solution, but instead focus on designing a ‘generalised inverse’ of the sensitivity matrix  $\mathbf{G}$ . We describe the SOLA method briefly below, with more details in Appendix A.

Let  $\mathbf{G}^\dagger$  be the ‘generalised inverse’ such that the model solution is expressed as linear combinations of the data:

$$\tilde{\mathbf{m}} = \mathbf{G}^\dagger \mathbf{d}. \quad (2)$$

Using Equation 1, we obtain a relation between the model solution and the ‘true’ model:

$$\tilde{\mathbf{m}} = \mathbf{G}^\dagger \mathbf{G} \mathbf{m}. \quad (3)$$

Each parameter in the model solution is a linear combination of the ‘true’ model parameters linked by the resolution matrix  $\mathbf{R} = \mathbf{G}^\dagger \mathbf{G}$ . In other words, the value of a model parameter in the model solution represents a spatial weighted average of the whole ‘true’ model (plus some errors propagated from data noise). The resolution for a model parameter is determined by this averaging and is referred to as ‘resolving’ or ‘averaging kernel’. In general, we prefer the averaging for a model parameter to be focused around that parameter location. The full resolution matrix thus acts as a ‘tomographic filter’ (e.g. [Ritsema et al., 2007](#); [Schuberth et al., 2009](#); [Zaroli et al., 2017](#)). Note that in the hypothetical case where the data geometry constrains all model parameters perfectly, the sensitivity matrix  $\mathbf{G}$  is invertible, the generalised inverse  $\mathbf{G}^\dagger$  is the exact inverse, the resolution matrix is the identity matrix, and, in the case of error-free data, the model solution is exactly the ‘true’ model.

Since  $\tilde{\mathbf{m}} = \mathbf{G}^\dagger \mathbf{d}$  is a linear mapping of a multivariate normal distribution, we obtain the model covariance matrix from the data covariance matrix using:

$$\mathbf{C}_{\tilde{\mathbf{m}}} = (\mathbf{G}^\dagger) \mathbf{C}_d \mathbf{G}^{\dagger T}, \quad (4)$$

where  $T$  denotes the matrix transpose. The diagonal elements of the model covariance matrix are the standard deviations of the model parameters, i.e.  $\sigma_{\tilde{\mathbf{m}}(k)} = \sqrt{\mathbf{C}_{\tilde{\mathbf{m}}}^{kk}}$ . Analogue to the data uncertainty, we refer to the model standard deviations as the model uncertainty. Note that model uncertainties are thus given for local



average estimates, not estimates at absolute points in space. In summary, the generalised inverse  $\mathbf{G}^\dagger$  determines the model solution, model resolution, and model uncertainty.

While data-misfit approaches have many advantages (e.g. treatment of non-linearity, computational efficiency), they do not directly control the resolution and uncertainty of the solution; estimating this information can be challenging depending on the inverse method used. With the SOLA method, which is based on Backus-Gilbert theory (Backus and Gilbert, 1967, 1968, 1970; Pijpers and Thompson, 1992, 1994; Zaroли, 2016), we explicitly design  $\mathbf{G}^\dagger$  to achieve certain objectives regarding the resolution and model uncertainty. In particular, we design a target resolution  $T$  and seek a generalised inverse that leads to a resolution as close as possible to the target, while minimising model uncertainty. These are two contradictory objectives that are balanced in an optimisation problem:

$$\begin{aligned} \mathbf{G}^\dagger^{(k)} &= \arg \min_{\mathbf{G}^\dagger^{(k)}} \sum_j [A_j^{(k)} - T_j^{(k)}]^2 \mathcal{V}_j + \eta^{(k)^2} \sigma_{m^{(k)}}^2, \\ \text{s.t. } \sum_j R_j^{(k)} &= 1, \end{aligned} \quad (5)$$

where  $k$  is the index of the model parameter for which we are solving (the target),  $j$  is a dummy index that iterates over model parameters,  $\mathcal{V}_j$  is the volume of cell  $j$ ,  $A_j^{(k)} = R_j^{(k)} / \mathcal{V}_j$  is the averaging (or resolving) kernel (normalised by the cell volume), and  $\eta^{(k)}$  is a trade-off parameter that balances the fit to the target resolution with the minimisation of model uncertainty. The constraint  $\sum_j R_j^{(k)} = 1$  guarantees that local averages are unbiased. This is important because an uneven data distribution can artificially increase or decrease the value of the estimated parameters, as demonstrated by Zaroли et al. (2017). The optimisation problem leads to a set of equations (see Appendix A1 from Zaroли, 2016) that we solve for each model parameter using the LSQR algorithm of Paige and Saunders (1982), as suggested by Nolet (1985).

The SOLA inversion is point-wise, i.e. the minimisation problem is solved for each parameter independently from the others. This makes SOLA inversions straightforward to solve in parallel. Note that we do not need to solve for all model parameters nor do we need to solve for the whole region to which the data are sensitive (a necessity in data-fitting inversions): we have the possibility to solve only for model parameters of particular interest (the targets). Furthermore, note that the data  $d$  do not appear in the optimisation equation 5. We provide information on the computational costs of this study in Appendix C.

### 2.3 Finite-frequency forward theory

In order to make the implementation of SOLA for surface-wave tomography fully three-dimensional, we need a linear relation between surface-wave data and 3D physical properties of the Earth mantle. Here, we consider as data vertical-component Rayleigh-wave

phase delays  $\delta\phi_l(\omega)$  measured at frequencies  $\omega$  for particular source-receiver pairs  $l$ . If we assume these delays are primarily sensitive to perturbations in the vertically polarized  $S$ -wave velocity  $\delta V_{SV}$  in the 3D mantle  $\oplus$ , we have the following relationship between data  $\delta\phi_l(\omega)$  and model  $\delta \ln V_{SV}(\mathbf{x})$ :

$$\delta\phi_l(\omega) = \iiint_{\oplus} K_l(\omega; \mathbf{x}) \delta \ln V_{SV}(\mathbf{x}) d^3\mathbf{x}, \quad (6)$$

where  $\mathbf{x}$  indicates the location, and  $K_l(\omega; \mathbf{x})$  is the sensitivity kernel. We neglect the sensitivity to other physical parameters (e.g.  $V_{SH}$ ,  $V_{PV}$ , density), but this contributes to the theoretical errors.

Analytical expressions of surface-wave sensitivity kernels have been derived based on the scattering principle in the framework of normal mode theory. Here, we use formulations from Zhou et al. (2004), later extended to multimode surface waves and anisotropy by Zhou (2009b). These assume far-field propagation, single forward scattering, and use a paraxial approximation. Thanks to the single-scattering assumption, also known as Born approximation, the resulting relationship between data and model is linear, which makes it tractable with SOLA. Single-scattering is equivalent to neglecting terms of order higher than 1 in the Taylor expansion of the Green tensor perturbations with respect to structural parameters (e.g. Dahlen et al., 2000). This single-scattering approximation also contributes to the theoretical errors. In this study, we restrict ourselves to fundamental modes, but extension of the theory to overtones is straightforward. The sensitivity kernels for the fundamental modes can be expressed as:

$$K(\omega; \mathbf{x}) = \text{Im} \left( \frac{S' \Omega R'' e^{-i[k'\Delta' + k''\Delta'' - k\Delta + (s' + s'' - s)\frac{\pi}{2} + \frac{\pi}{4}]} }{S R \sqrt{8\pi \left(\frac{k'k''}{k}\right) \left(\frac{|\sin|\Delta'| |\sin|\Delta''|}{|\sin|\Delta|}\right)}} \right). \quad (7)$$

Symbols with prime ' refer to the source-scatterer path, ones with double prime '' to the scatterer-station path, and those without prime to the great-circle source-station path;  $k$  is the wave-number and  $s$  the Maslov index (here  $s = 0$  or  $s = 1$ , i.e. single orbit);  $\Delta$  is the path length,  $S$  the source radiation in the direction of the path, and  $R$  the projection of the polarisation onto the receiver orientation. The exponent term indicates the phase delay due to the detour by the scatterer, while the other terms express the relative amplitude of the scattered wave relative to the initial unperturbed wavefield. This relative strength depends on the source and receiver terms (the scattered wave leaves the source and arrives at the receiver with some angle compared to the unperturbed wave), on the geometrical spreading (the scattered wave makes a detour compared to the unperturbed wave), and on the scattering coefficient  $\Omega$ . The scattering coefficient depends linearly on physical model properties, for which detailed expressions can be found in Zhou (2009a). In practice, we use a slightly different form of Equation 7 to include the effect of wave-form tapering in the measurement algorithm (see Zhou et al., 2004, for more details).

We use routines from Zhou (2009b) to compute the sensitivity kernels for the fundamental mode, assum-

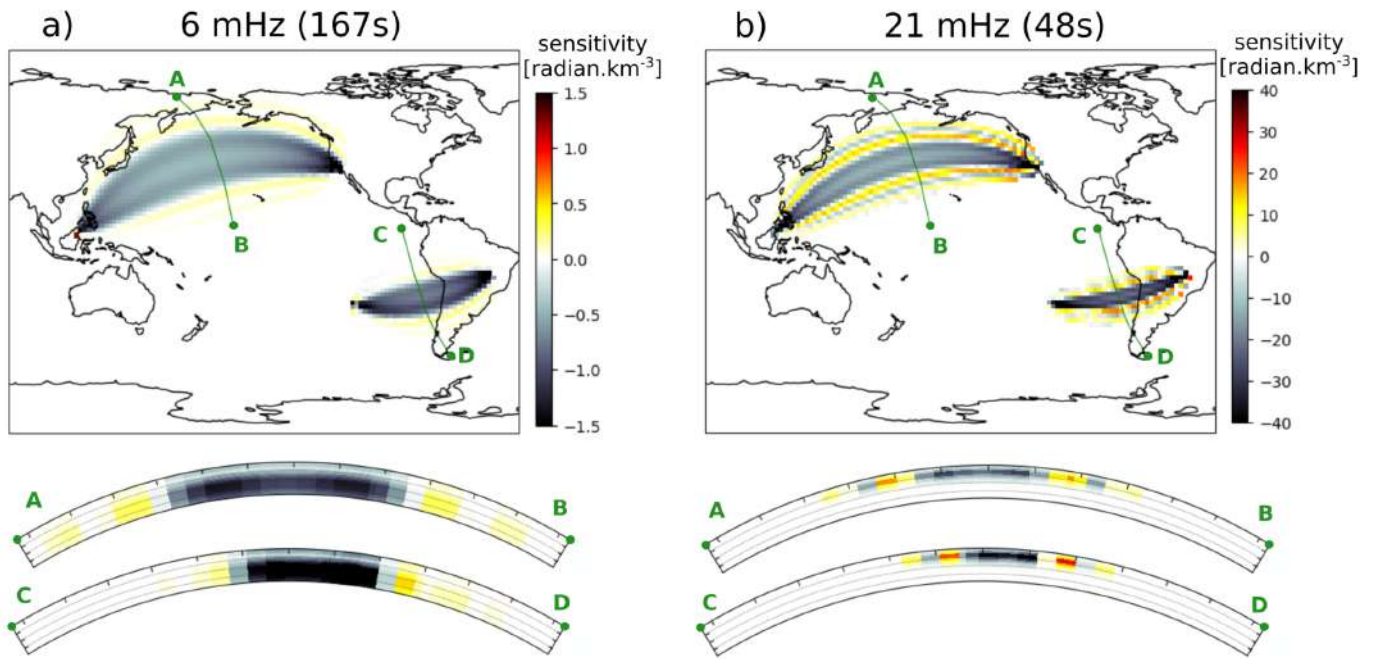


**Figure 1** Examples of sensitivity kernels at a) 6 mHz and b) 21 mHz for two source-receiver pairs. The maps are plotted at depths of 87 km and 237 km depth respectively, which are the depths where the kernels reach their respective maximum amplitudes. Below each map, we also show a vertical cross-section through each kernel, as indicated on the maps, and the dotted lines indicate depths of 100, 200 and 300 km. The northern kernel is for a  $M_w$  6.1 earthquake in Borneo (2015) recorded by station DSN5. The southern kernel is for a  $M_w$  6.1 earthquake in the Easter Island region (2011) recorded by station BDFB. Note the difference in amplitude between the two frequencies shown in a) and b).

ing self-coupling. We only compute these in the top 400 km of the mantle as their amplitude decreases sharply with depth. We consider the first two Fresnel zones laterally as their side-lobes become negligible further away. Examples of sensitivity kernels are given in Figure 1, where they are projected onto the tomographic grid. The kernels have particularly strong amplitude at the source and station. This is caused by a combination of natural high sensitivity at end-points of a path and the far-field approximation (e.g. Liu and Zhou, 2016b). Low-frequency kernels peak at deeper depths, have a broader lateral and vertical extent, and have weaker amplitudes than high-frequency kernels. Although the projection onto the tomographic grid degrades the shape and amplitude of the sensitivity kernels, their main properties are retained on a tomographic grid that is sufficiently fine.

### 3 Tomography setup

In this section, we present the construction of the forward problem (the sensitivity matrix) and the inverse solution (the generalised inverse) that determines the resolution, the propagation of data uncertainty into model uncertainty, and the propagation of data values into model estimates. We will describe the data and data uncertainty in the next section. These will feed into the inverse solution to produce the tomography model and the measurement model uncertainty.

#### 3.1 Parameterisation

We use a local model parameterisation and split the 3D spatial domain into voxels of size  $2^\circ \times 2^\circ$  laterally (latitude and longitude) and 25 km depth vertically. We parameterise the whole sphere laterally, but only the top 400 km depth, since the sensitivity of fundamental mode surface waves to  $V_{SV}$  becomes negligible at greater depths. This leads to  $M = 259\,200$  voxels. It is worth recalling that with SOLA we do not need to solve for all  $M$  model parameters nor for the whole region to which the data are sensitive. For example, we could solve only for cells where the data sensitivity is sufficiently high or only for a particular region of interest. Note that the parameterisation does not impact the SOLA inversion in the same way as in data-fitting approaches. Primarily, the parameterisation should be chosen finer than the target kernels if these are to be honoured. However, the parameterisation is expected to have an impact on the theoretical uncertainty, as the discretisation of the sensitivity kernels degrades the accuracy of the forward theory.

#### 3.2 Data geometry

We select 312 earthquakes with  $M_w$  between  $\sim 6.0$  and 7.7 and depth between  $\sim 12$  and 87 km, all located in the Pacific region, occurring between July 2004 and December 2020. We consider 1228 stations, also located in the Pacific region (see Fig. 2). Sources and stations are both selected in a way to avoid strong spatial redundancy. For all paths, we consider 16 frequencies ranging from 6 to 21 mHz (48-167s), in steps of 1 mHz.



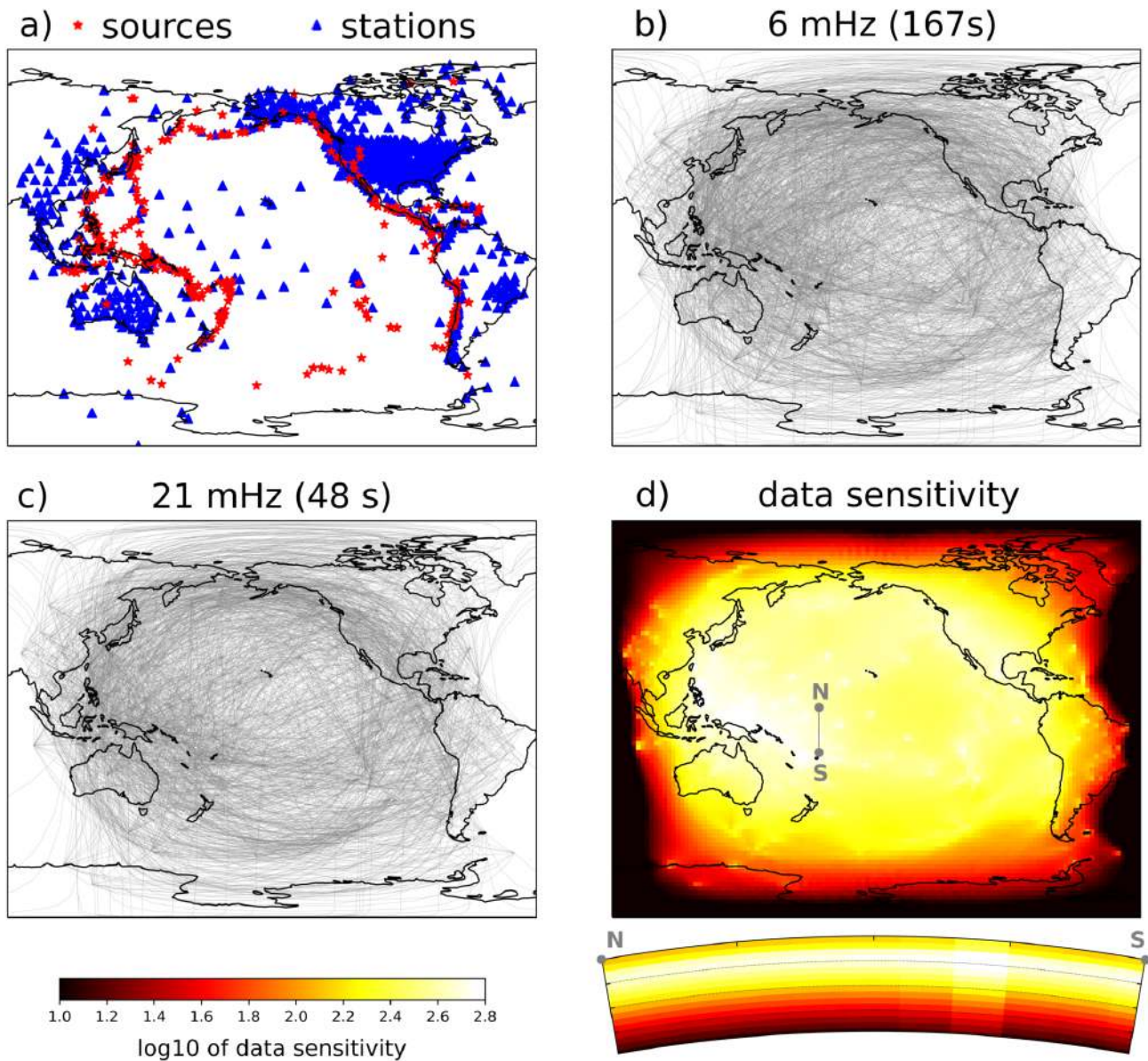


**Figure 2** Data geometry of our tomography, showing a) the distribution of sources and receivers, b) the selected ray paths at 6 mHz and c) at 21 mHz, and d) the decimal logarithm of the data sensitivity,  $\log_{10} \sum_i |G_{ij}|$ . The data sensitivity is plotted at 112 km depth, with a N-S oriented vertical cross-section below it, indicated by the grey line on the map view, and the dotted lines indicate depths of 100, 200 and 300 km.

Compared to ray-theory, finite-frequency theory is fully three-dimensional. This makes the sensitivity matrix larger because we need to consider the whole 3D spatial extent of the model domain all at once, and less sparse because finite-frequency sensitivity kernels have a volumetric extent. Since we store the whole sensitivity matrix in RAM to favour fast computation, this is a challenging issue that limits the number of data we can take into account in the inversion. For a computational node with 254 GB of RAM, and our current strategy for storing matrices in RAM, we estimate that we can incorporate at most  $N = 300\,000$  measurements (more information on the computational costs of this study is given in Appendix C). Here, we restrict ourselves to  $N \approx 50\,000$  measurements, making it possible to expand our work to overtones in the future. To achieve  $N \approx 50\,000$  data, we carefully select our data with the aim to homogenise

the lateral distribution of rays (see Section 4). We end up with 47,700 data in total, with approximately 3,000 data per frequency (Figure 2).

For each selected measurement, we compute the corresponding 3D finite-frequency sensitivity kernel to build the sensitivity matrix  $G$ , with examples shown in Figure 1. As a measure of the constraint offered by the data on the structure of the 3D upper mantle, we compute the decimal logarithm of the data sensitivity,  $\log_{10} \sum_i |G_{ij}|$ , where  $i$  and  $j$  designate a particular datum and model parameter respectively (see Figure 2, lower right).

### 3.3 Target resolution, uncertainty propagation, and their trade-off

The shape of the target kernels used in the SOLA inversion is arbitrary. Ideally, it is chosen such as to produce

results oriented towards addressing a specific key question (e.g. Mag et al., 2025). In this study, we wish for the resolution to represent simple, easy-to-interpret 3D local averages. For a given model parameter, we therefore choose the target kernel to be a 3D ellipsoid. The lateral resolution we can achieve with surface-wave data is controlled by the distribution of sources and receivers (and, to some extent, frequency). Our experience shows that it is rarely better than a few hundreds of kilometres for the frequency range used here. The vertical resolution is mostly controlled by the frequency content of the signal and it is typically on the order of tens to hundreds of kilometres. Therefore, a reasonable target kernel at a given point in the 3D grid would resemble a thick pancake centred at the query point. More formally, we design the target kernel of a model parameter as an ellipsoid whose major and intermediate axes are equal and aligned with the north-south and east-west directions at the location of the model parameter, and whose minor axis is vertical. The resulting target kernels are thick versions of the 2D kernels of Lattalier et al. (2022) and Amiri et al. (2023) and they represent a horizontally isotropic target resolution.

With SOLA, it is possible to adapt the size of the target kernels for each model parameter (i.e. for each location). For example, we could choose to achieve the best resolution possible at each location in the model given the data coverage, or we may prefer a homogeneous resolution or constant uncertainty across the spatial domain (see Freissler et al., 2024). This freedom illustrates the typical non-uniqueness of tomographic inversions. We could compute an L-curve for the resolution size versus model uncertainty to choose an optimal trade-off parameter. However, this L-curve would have a very different meaning than that computed for data-fitting approaches that typically consider data-fit versus model smoothness. With SOLA, we do not need to compute an L-curve as any choice of the trade-off parameter that fits the purpose of the study can be considered ‘good’, so long as the tomographic model is analysed together with its resolution and uncertainty (see also supporting information of Zaroli et al. (2017)). In this study, for simplicity, we make all target kernels the same, with 200 km long horizontal major and semi-major axes and 25 km long vertical minor axis. Figures 3 and 4 illustrate the extent of our target kernels for 10 different locations (blue ellipses).

The data uncertainty could influence the generalised inverse we obtain with SOLA through the second term in the optimisation problem in Equation 5. However, as we aim to study the robustness of the data uncertainty itself in this study, we decide not to take it into account in designing  $G^\dagger$ . Thus, we initially set  $C_d = I$  and therefore  $C_m^\sim = (G^\dagger)^T G$ . This choice is only for designing  $G^\dagger$ : once the generalised inverse has been computed, we propagate the actual measurement uncertainty into model uncertainty through  $C_m^\sim = (G^\dagger)^T C_d G$ . Depending on the application, different data weighting (including data uncertainty), could be considered to produce an optimal generalised inverse.

The optimisation problem involves the minimisation of the difference between target and actual resolution

on the one hand, and the magnitude of model uncertainty on the other hand. These two terms are balanced by the trade-off parameter  $\eta$ , which we set equal to 50 for all parameters. Again, it is possible to choose different values of  $\eta$  for different model parameters, but in practice it is computationally easier to keep  $\eta$  constant (see Appendix A1 of Zaroli, 2016). If, for example, one wants to give more weight to the resolution of a particular model parameter, this can also be obtained by designing a smaller size target kernel. If we vary the trade-off parameter, we obtain a typical L-shaped trade-off curve for resolution versus model uncertainty for each target (Lattalier et al., 2022; Restelli et al., 2024).

### 3.4 Generalised inverse: Resolution and uncertainty propagation

The seismic tomography inversion is fully characterised by the generalised inverse  $G^\dagger$ : it determines the resolution (from  $R = G^\dagger G$ ) as well as the propagation of data uncertainty into model uncertainty (from  $C_m^\sim = (G^\dagger)^T C_d G^\dagger$ ). Lastly, it determines the propagation of data into model solution (from  $\tilde{m} = G^\dagger d$ ).

It is difficult to represent the full 3D resolution as it is most easily understood in terms of an extended 3D resolving kernel associated with each model parameter. A detailed analysis thus requires 3D rendering software or the production of simple proxies, for example those proposed by Freissler et al. (2024). Here, we instead illustrate the resolution by selecting example resolving kernels. At 112 km depth (Figure 3), the resolving kernels match the target location well laterally. Their lateral size is roughly 250-450 km (if we take the radii of a circle containing 68% of the kernel). This can be compared to the length of the major and intermediate axes of the target kernels of 200 km. Some averaging kernels are significantly anisotropic, indicating lateral smearing due to the heterogeneous ray path distribution. Vertically, the resolving kernels appear also to be focused with a half-thickness of roughly 50 km. This can be compared to the length of the minor axis of the target kernels of 25 km. However, they appear slightly shifted upward from the target. Deeper down, at 212 km depth (Figure 4), the resolving kernels still match the target locations laterally, but they appear broader (300-700 km). They now also poorly match the target kernel depth-wise. Instead of peaking at 212 km depth, the resolving kernels peak at 112 km depth and tail off deeper down. This implies that what we observe in the tomographic model at 212 km depth is actually an average of the ‘true model’ at shallower depth.

We show the ‘error propagation factor’ in Figure 5. This can be interpreted as the model uncertainty for unit data uncertainty ( $C_d = I$ ), obtained from  $(G^\dagger)^T G^\dagger$ . We observe a positive correlation between data coverage and error propagation factor: the error propagation tends to be high where data coverage is high (e.g. North America, South-East Asia). We also clearly see patches of high error propagation in the Pacific Ocean at locations of isolated stations. This is due to the high data sensitivity at stations where many oscillatory sensitivity kernels add together. Further-



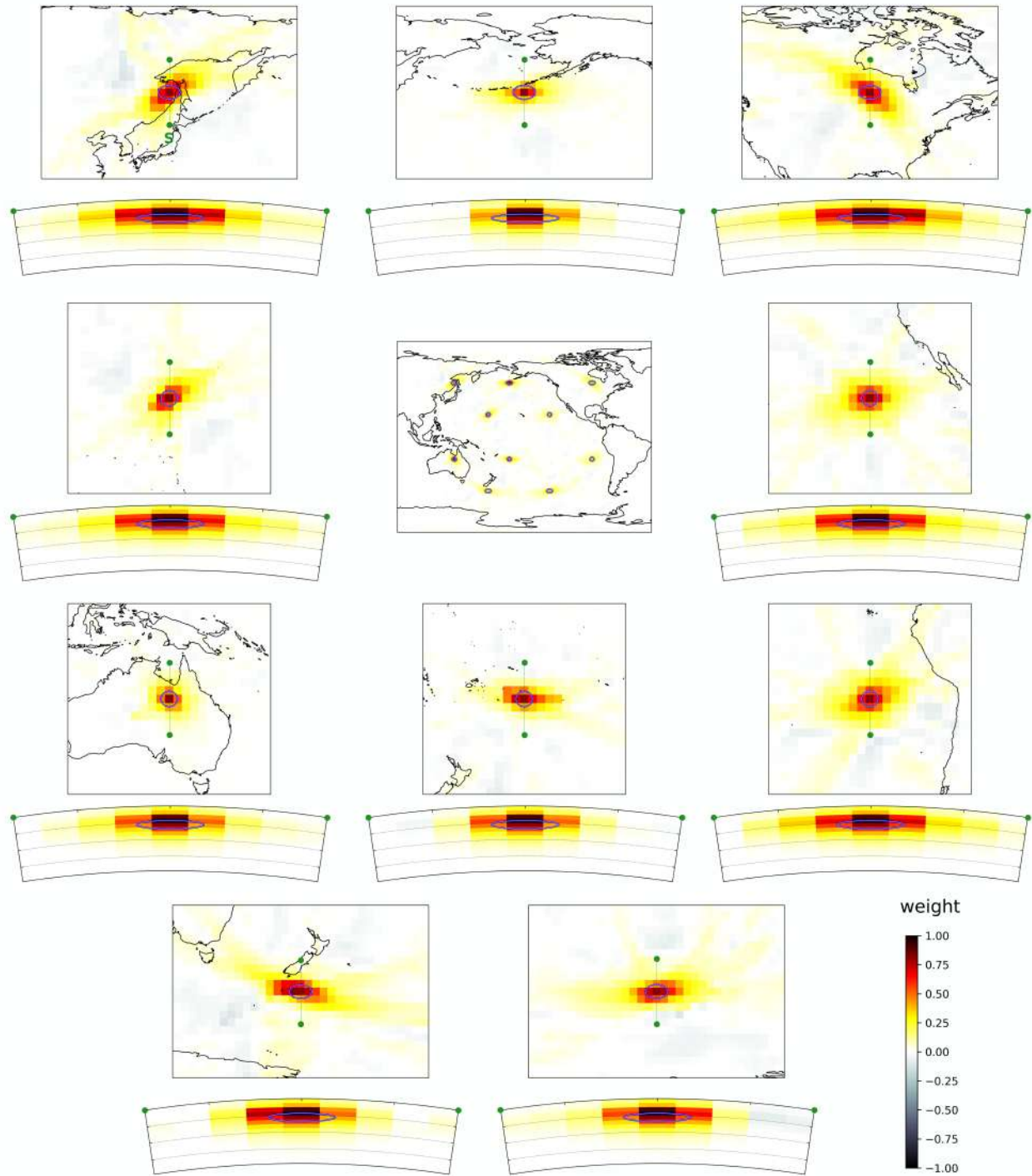


**Figure 3** Resolution at 112 km depth illustrated for a selection of 10 model parameters. The centre map shows the locations of the 10 target and resolving kernels. This is shown as a sum, which may exaggerate the apparent strength of the tails. The surrounding panels are close-ups on individual kernels, both in map-view and as cross-section. All maps represent depth slices at 112 km depth and below each map is a  $\sim 3100$  km long, N-S oriented (left to right) cross-section as indicated in green in the maps, with the dotted lines indicating depths of 100, 200 and 300 km. Blue ellipses show the lateral extent of the target kernels. All averaging kernels are normalised by their maximum, and the color scale indicated in the lower right applies to all panels.



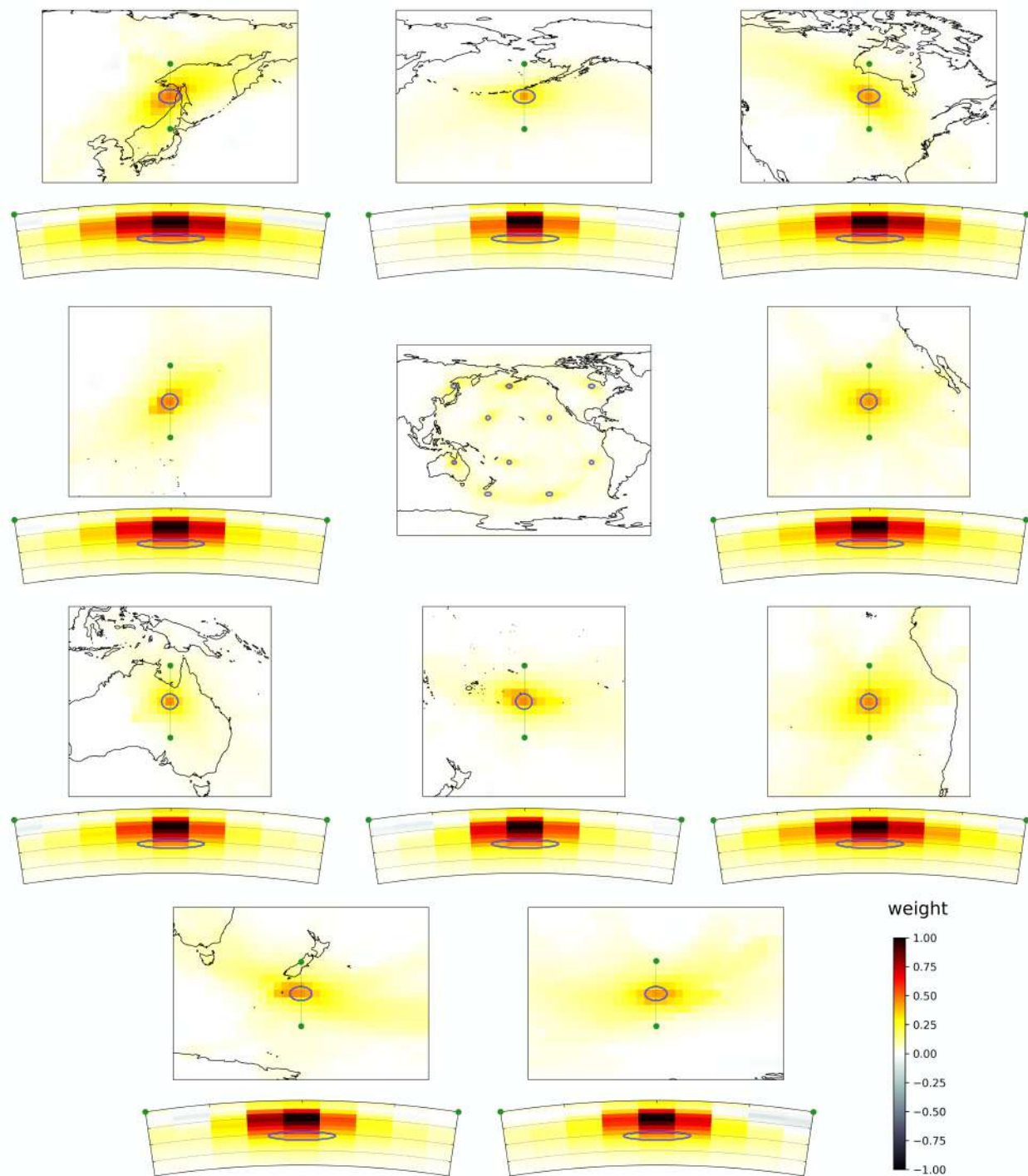


**Figure 4** Same as Figure 3, but for target locations at 212 km depth.

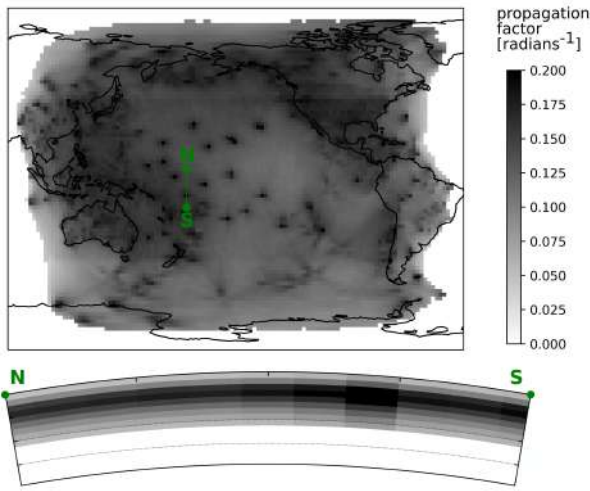


**Figure 5** Illustration of the propagation of data uncertainty into model uncertainty. The map shows the ‘propagation factor’ at 112 km depth, defined as the model uncertainty given unit data uncertainty. The cross-section below the map indicates the depth dependence of the propagation factor along a vertical 2500-km long N-S oriented profile as indicated by the green line on the map, with the dotted lines indicating depths of 100, 200 and 300 km.

more, we note linear features with high error propagation that follow great-circle paths radiating away from some isolated stations. These probably outline sensitivity kernels that repeatedly sample similar regions. With depth, we find that the propagation factor increases down to 87 km depth and then decreases again deeper down. While this decrease may seem surprising, it is balanced by poor resolution at greater depth. In general, SOLA tends to produce models with better resolution where data sensitivity is high, at the cost of a larger error propagation factor. By choosing different sizes for the target kernels, this can be balanced (Freissler et al., 2024).

## 4 Input data and measurement uncertainty

We measure phase delays between ‘observed’ and ‘reference’ seismograms for 16 different frequencies ranging from 6 to 21 mHz (48-167s), in steps of 1 mHz. In this synthetic study, we use as ‘observed seismograms’ waveforms computed using SPEC-FEM3D\_GLOBE (Komatitsch and Vilotte, 1998; Komatitsch and Tromp, 2002) for the 3D input model S362ANI (Kustowski et al., 2008) combined with CRUST2.0 on top (Bassin et al., 2000). Hereafter, we refer to these as SEM seismograms or SEM measurements. They were obtained from the GlobalShakeMovie project data base (Tromp et al., 2010) and downloaded from Earthscope, formerly IRIS (IRIS DMC, 2012; Hutko et al., 2017). Reference seismograms were computed using normal-mode summation with the Mineos software (Masters et al., 2011) for the 1D radial model stw105 (Kustowski et al., 2008), consistent with S362ANI. For both sets of seismograms, we use

source solutions obtained from the Global-CMT project (Ekström et al., 2012) and station metadata from Earthscope. To measure the phase delay between the two sets of seismograms, we use a multi-taper measurement algorithm as suggested by Zhou et al. (2004) and detailed in appendix B. The multi-taper technique has the advantage of providing an estimate for the measurement data uncertainty as the standard deviation of the measurements across all tapers. This uncertainty estimate is particularly sensitive to cycle-skipping and contamination by higher modes and other phases.

Considering only source-receiver combinations for which the measurement time window (150 s before to 650 s after the predicted group arrival time) does not include the event origin time, we obtain 2,414,515 measurements of Rayleigh wave phase delays. We select a subset of these measurements based on the following criteria: similarity between the seismograms (cross-correlation  $> 0.8$ ), source radiation in the direction of the station ( $> 80\%$  of maximum radiation), measurement uncertainty ( $< 1.9$  radians), outlier removal (1% of the dataset). This leads to 564,940 potential measurements. Due to memory limitations (as explained in section 3.2), we select a subset of  $N = 47,700$  data to reduce the size of  $G$ . This is achieved by randomly selecting one ray, then removing all rays whose endpoints are within 800 km radius of the endpoints of the selected ray, and repeating this process until we reach the desired number of measurements, at the frequency of interest. This gives the vector of measured data that we denote  $d^{\text{measured}}$ . Other approaches, such as ‘bootstrapping’ or ‘summary ray’ techniques could be experimented with to further investigate the uncertainty in the dataset or to compare to the uncertainty that we obtain with the multitaper technique. As a check, we also compute the corresponding analytical data  $d^{\text{analytical}}$  by applying our forward theory  $G$  to the 3D input model S362ANI ( $m^{\text{input}}$ ), i.e.  $d^{\text{analytical}} = Gm^{\text{input}}$ .

The inversion for crustal structure is highly non-linear and often avoided in surface-wave tomography. SOLA cannot handle this non-linearity and we therefore apply a crustal correction to our measurements (e.g. Marone and Romanowicz, 2007; Bozdağ and Trampert, 2008; Panning et al., 2010; Liu and Zhou, 2013; Chen and Romanowicz, 2024). For consistency with the synthetic ‘observed’ waveforms, we also use CRUST2.0 to compute the crustal correction (Bassin et al., 2000). We first construct 1D radial models for a combination of stw105 and CRUST2.0 at every location in a  $2^\circ \times 2^\circ$  grid. For each grid point, we then solve a normal-mode eigenvalue problem using Mineos (Masters et al., 2011) to obtain the local phase velocity, thus building phase velocity maps for the reference model with the added crustal structure. For each source-receiver path and all frequencies in our dataset, we subsequently compute the phase accumulated in this model  $\phi^{\text{ref+crust}}$  as well as in the reference model  $\phi^{\text{ref}}$ , assuming ray-theory (i.e. great-circle approximation). The difference in phase due to the crustal structure  $\delta\phi^{\text{crust}} = \delta\phi^{\text{ref}} - \delta\phi^{\text{ref+crust}}$  is then used to correct the measured data:  $d^{\text{corrected}} = d^{\text{measured}} - \delta\phi^{\text{crust}}$ .

Examples of our dispersion measurement procedure

and results are given in Figure 6 and used to illustrate three typical cases. In Case I (left column), measurements agree well with the analytical predictions and have low uncertainty. In Case II (middle column), measurements do not agree well with the analytical predictions, but this is compensated by high data uncertainty. In Case III (right column), which is more problematic, the measurement has low uncertainty, but it does not match the analytical prediction. In this example, it appears that the cycle-skip correction (see Appendix B) has failed to detect a cycle-skip at 8 mHz. Since the measurements are consistent for all tapers, the uncertainty estimation fails to pick-up the cycle-skip and the uncertainty remains low. Therefore, the final measurement includes a cycle-skip difference with the analytical data above 8 mHz that is not reflected in the uncertainty. This is relatively common in surface-wave tomography (e.g. Moulik et al., 2021). Even if we could spot measurements with cycle-skips in a synthetic tomography setup, we do not remove them from the dataset to mimic a real case application. Note that discrepancies between analytical predictions and measurements are due both to errors in the measurement (poorly measured data), as well as to errors in the forward theory (poor analytical data). At this stage, we ignore uncertainty arising from theoretical errors.

To get a feeling of the volume of data falling in each of these three cases, we define three classes based on the difference between analytical prediction and measurement: (i) below 3 radians and within 3 standard deviations for Class I; (ii) above 3 radians and within 3 standard deviations for Class II; and (iii) above 3 radians and outside 3 standard deviations for Class III. For completeness, we also define Class IV as below 3 radians and outside 3 standard deviations. Classes I, II, III and IV contain respectively 27%, 1%, 43%, and 29% of the dataset. In other words, 27% of the dataset show a good agreement between the predictions and measurements and this difference is also within 3 times the measurement uncertainty. 1% of the data does not show a good agreement (i.e. above 3 radians), but is still within 3 times the measurement uncertainty. 43% shows poor agreement and is also outside 3 times the measurement uncertainty, and 29% is in good agreement, but outside 3 times the measurement uncertainty (indicating a small uncertainty). In summary, 56% of the dataset shows good agreement (class I and IV), and 28% has a difference smaller than the measurement uncertainty (class I and II). Note that the boundaries of these classes, namely the threshold of 3 radians and 3 standard deviations, are somewhat arbitrary and primarily given to provide a sense of the data volume falling within each case illustrated in Figure 6.

Figure 7 presents statistics summarising our measurements and associated uncertainty. Our measured phase delays are typically larger than the analytical predictions ( $d^{\text{analytical}} = Gm^{\text{input}}$ ) for both positive and negative delays, possibly due to non-linear effects. We may therefore expect increased positive and negative anomalies in our resulting tomographic model. We also observe a parallel branch of negative measured phase-delays with respect to the analytical predictions, likely

due to non-detected cycle-skips. Our measurement uncertainty peaks around 0.3-0.5 radians, with the peak uncertainty shifting to higher values (to the right) for higher frequencies (darker colours). The effect of this shift on the resulting model uncertainty is not easy to predict as different frequencies impact the model solution in different ways (e.g. low frequency data have overall lower sensitivity). We also observe two additional peaks for higher uncertainty values, probably due to cycle-skipping and contamination with higher modes. However, measurements with these uncertainty values are not included as we apply a cut-off of 1.9 radians in our data selection. We also observe a spatial pattern in the deviation between analytical and measured data in panels c) and d). Higher differences tend to be found for rays along ridges or along the ocean-continent boundaries. High deviations are also found in the central Pacific at lower frequencies. These may be due to limitations in the forward theory as non-linearities are to be expected for these regions.

We now have a dispersion data set with an estimate of the measurement uncertainty. While this measurement uncertainty provided by the measurement algorithm accounts for cycle-skips and contamination by other phases or higher modes, to some extent, it does not capture the theoretical errors. We estimate these in the following section.

## 5 Results

In the perfect case of error-free analytical data  $d^{\text{analytical}}$ , an inversion should produce a model solution that is exactly the same as the filtered input. We confirm that by comparing the analytical model solution  $\tilde{m}^{\text{analytical}} = G^\dagger d^{\text{analytical}}$  to the filtered input  $Rm^{\text{input}}$ . When we instead use the measurements on SEM waveforms  $d^{\text{corrected}}$ , differences between the filtered input model  $Rm^{\text{input}}$  (Figure 8b) and the obtained model solution  $\tilde{m}^{\text{output}}$  (Figure 8d) arise due to a combination of both measurement and theoretical errors. Only the former have been taken into account in the model uncertainty map shown in Figure 8c. Note how the edges of the model solution appear rough. This is because we invert only for model parameters where the data sensitivity is higher than a certain threshold (depending on depth); this is possible due to the point-wise nature of the SOLA inversion.

### 5.1 Qualitative proof of concept: velocity models

The features in the input model (Figure 8a) are also mostly present in the filtered model (Figure 8b). This indicates that the model resolution is good, at least at 112 km depth. For example, we retrieve mid-ocean ridges (low velocities at the East-Pacific rise, Pacific-Antarctic ridge, the edges of the Nazca plate), the lithosphere cooling effect (increasing velocity with distance from the ridge), the ring of fire (low velocity in the back-arc regions behind subduction zones such as the Aleutian trench, Okhotsk trench, edges of the Philippine sea plate and the Tonga-Kermadec trench), and cratons (fast



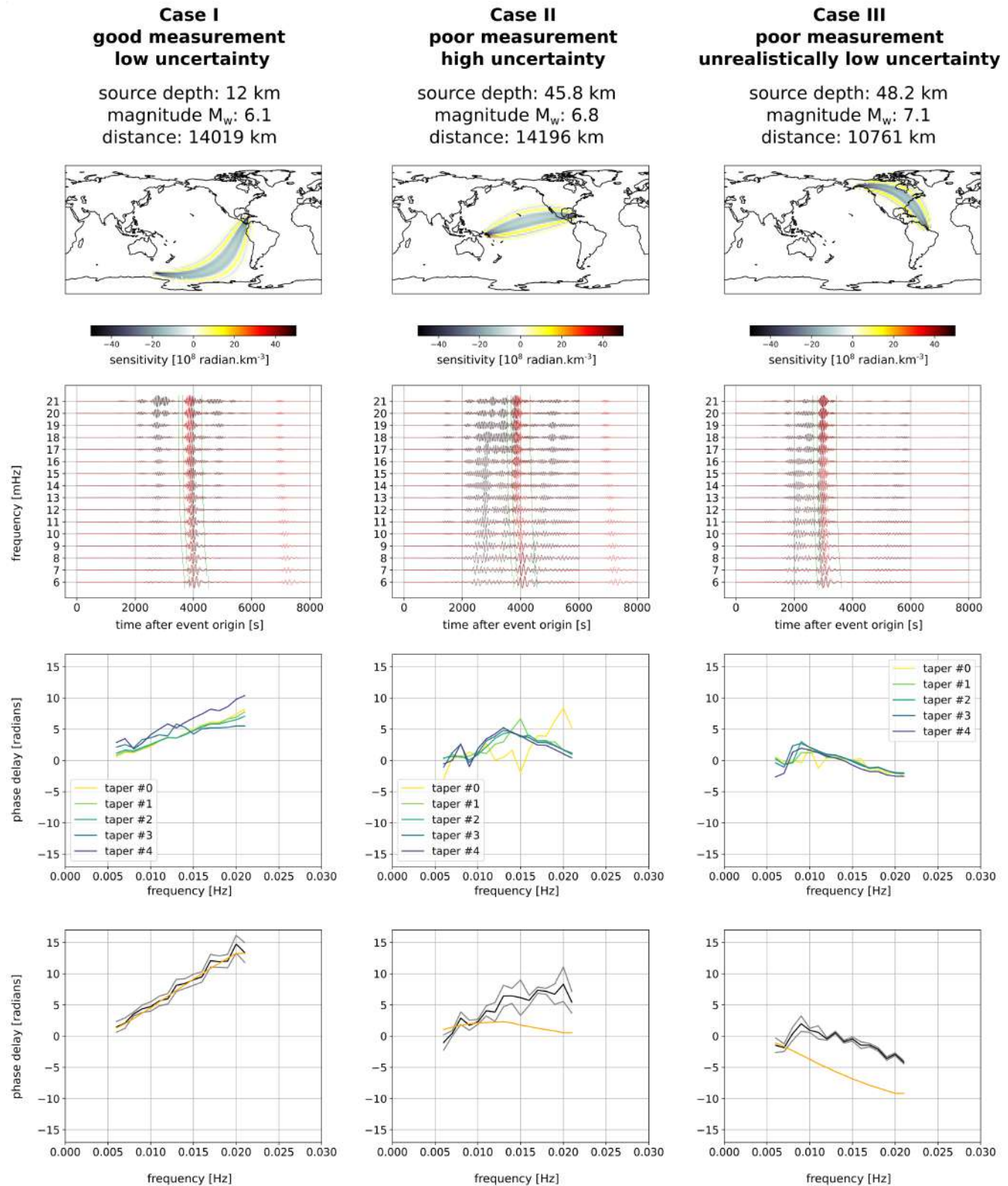


**Figure 6** Example dispersion measurements, showcasing three typical cases. For each case (column), we include the sensitivity kernel at 16 mHz, plotted at 112 km depth (top row); the seismic traces (second row) for 8000 s after the event origin time (reference in black, SEM in red), filtered around each measurement frequency, and the green vertical lines indicate the start and end times of the applied tapers, around the predicted group arrival time; the measured dispersion for each taper (third row); and the final dispersion measurement (bottom row) averaged over all tapers (black) with the estimated uncertainty (grey), compared with the analytical prediction (orange). In the last row, the crustal correction is also applied to the measurements.

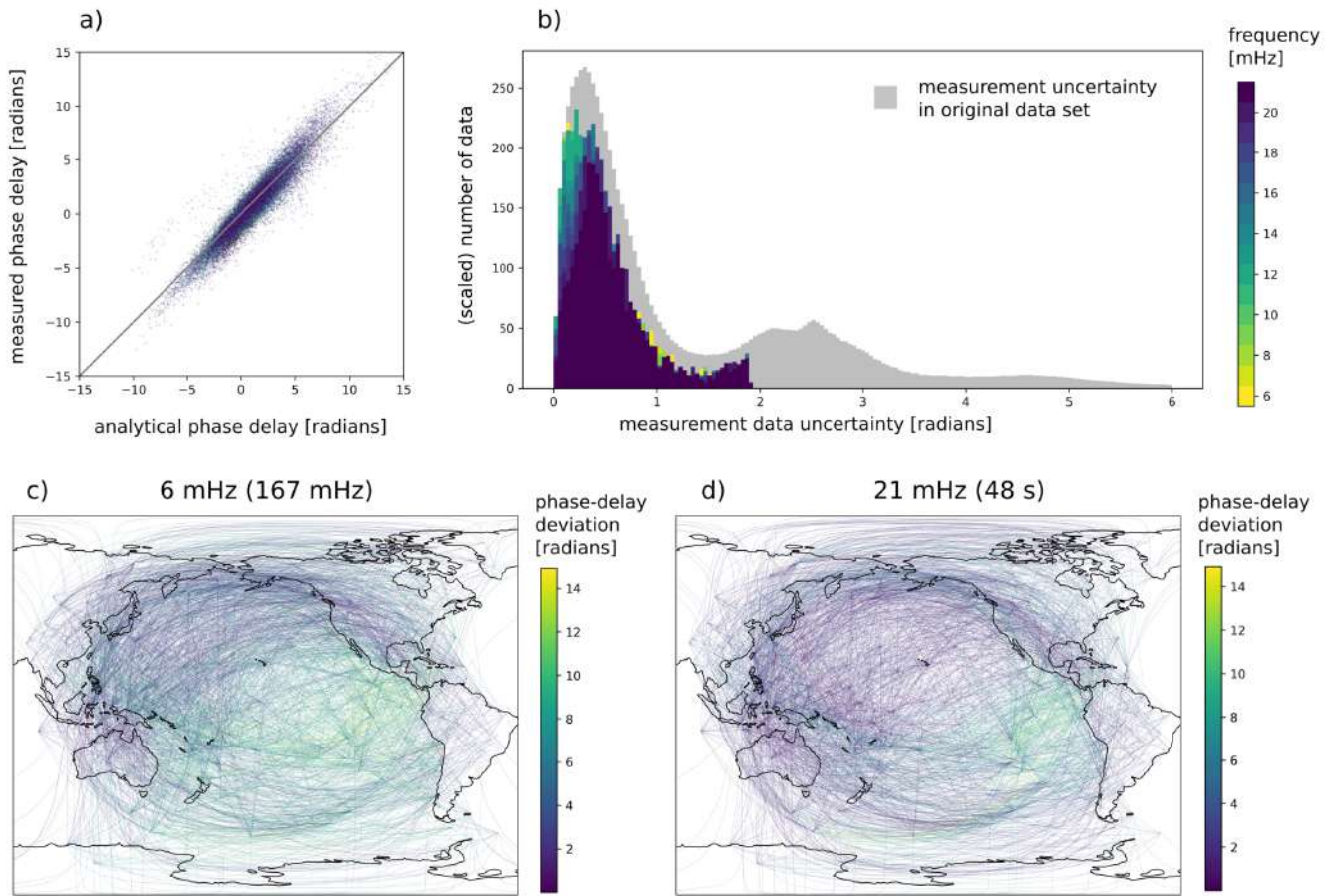


**Figure 7** Summary of data and measurement uncertainty. a): Cross-plot of the measured phase delay (after crustal correction) versus the analytical phase delay prediction, coloured by frequency. Positive phase-delays typically indicate slow velocity anomalies. b) Distribution of measurement data uncertainty (coloured by frequency) before (grey) and after applying several selection criteria. Our selection criteria include a threshold for the data uncertainty (lower than 1.9 radians), as visible in the plot. The distribution of the measurement uncertainty before applying the selection criteria is scaled by 0.003 to enhance its visibility. c) and d) ray-path distribution coloured by the deviation between analytical and measured phase delays at 6 mHz and 21 mHz respectively.

velocities within the Australian and North American continents). Note that *S362ANI* is a relatively smooth model, and we would probably miss smaller-scale features in a rougher model.

The amplitudes of the velocity anomalies in the filtered model are lower than in the input model. This is expected since the filtered model represents (unbiased) local averages (Zaroli et al., 2017). The filtered model is also rougher on short length scales compared to the input model. This can be explained by the local nature of SOLA inversions where each model parameter is inverted independently from the others. In this case, we notice this particularly because the input model itself is very smooth. Some artefacts appear such as the fast velocity anomaly of SW Australia extending through the slow velocity of the Australian-Antarctic ridge. Some striations also appear in the fast velocity region in the NW Pacific, trending in the SW-NE direction. These artefacts are probably the result of anisotropic ray coverage, with many sources in East-Asia mostly recorded by stations in North-America. In addition to these artefacts, some local features disappear in the filtered model, such as the low velocity finger extending

southward from the Aleutian trench, or the branch extending north-westward from Hawaii. Overall, the filtered input resembles the ‘true’ input model well, as also reflected in the cross-sections underneath.

The resulting model solution based on SEM seismograms (Figure 8d) appears very similar to the filtered input (Figure 8b), with differences between them shown in Figure 8e and f. Compared to the input and filtered input models described above, the model solution appears somewhat rougher due to the propagation of data errors into the model solution (Figure 8d). The striations observed in the NW Pacific in the filtered model are also stronger in the model solution than in the filtered input. The strongest spatially coherent discrepancies appear close to the East Pacific Rise, the North American Craton, and along the ocean-continent boundaries. These locations correlate well with the locations of ray paths of the most discrepant measurements (Figure 7). Finally, the cross-section indicates a good agreement between the filtered model and our model solution.



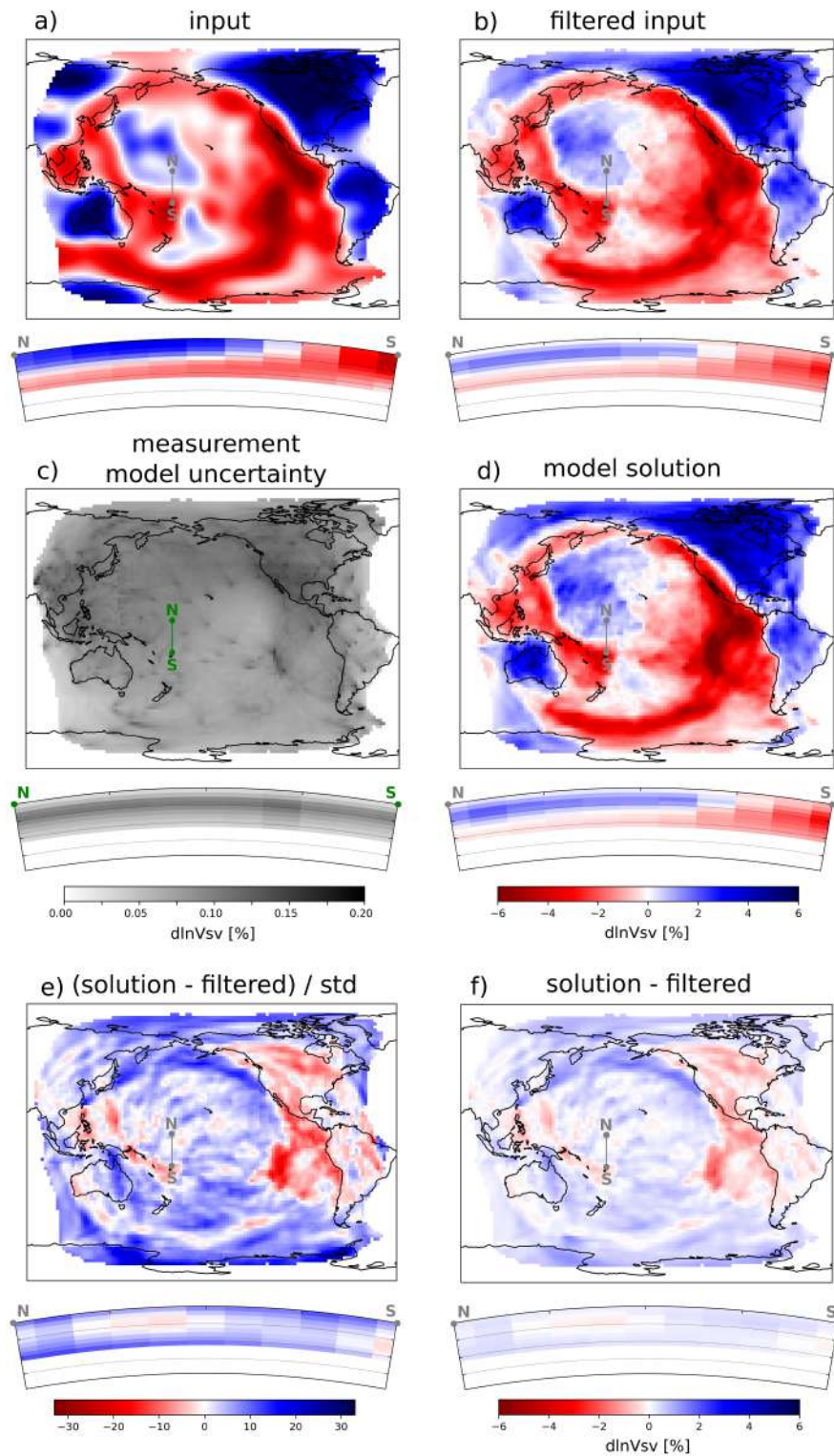


**Figure 8** Summary of synthetic inversion results, comparing a) input model S362ANI, b) input model S362ANI filtered using our resolution matrix, c) the model measurement uncertainty (propagated from data measurement uncertainty), and d) the model solution retrieved using the measured data values (based on the SEM seismograms), f) the difference between the model solution in d) and filtered input model in b), and e) same as f) but normalised by the model uncertainty. All maps represent depth slices at 112 km depth, as in Figure 3. Below each map is a N-S vertical cross-section with the location indicated by the grey or green line on the maps, and the dotted lines indicate depths of 100, 200 and 300 km.

## 5.2 Quantitative proof of concept: uncertainty

Our model measurement uncertainty map (Figure 8c) is very similar to the ‘uncertainty propagation factor’ map

in Figure 5. Uncertainty is typically higher where there are clusters of stations and at isolated stations with linear features following great circle paths. Uncertainty peaks at  $\sim 87$  km depth and decreases strongly at greater



depth. This uncertainty only stems from the data uncertainty, and is lacking the contribution from the theoretical uncertainty. Theoretical errors arise from a multitude of approximations as discussed in the Introduction. How much these contribute to the data uncertainty is generally difficult to determine, but using our setup we try to obtain some insights into the theoretical uncertainty and to inform future studies.

We propose the following strategy to estimate the magnitude of the theoretical model uncertainty. Let  $\mathbf{m}^{\text{input}}$  and  $\mathbf{m}^{\text{output}}$  be the input model and model solution respectively. Any discrepancy between the input model and model solution arises from the limited resolution and propagation of data uncertainty into model uncertainty. To rule out the effect of limited resolution, we apply the resolution to the input model to obtain the ‘filtered’ input model  $\mathbf{Rm}^{\text{input}}$ . Therefore, in this synthetic setup, it is only the propagation of measurement and theoretical errors into model errors that explains the discrepancy between the ‘filtered’ input model and the obtained model solution. This is confirmed by the fact that the model solution based on error-free analytical data reproduces the filtered input exactly. Let us define the model misfit normalised by the model uncertainty as:

$$\xi_m^2 = \sqrt{\frac{1}{\sum_{k \in \mathcal{P}} V_k} \sum_{k \in \mathcal{P}} V_k \frac{[(\mathbf{m}^{\text{output}})_k - (\mathbf{Rm}^{\text{input}})_k]^2}{(\sigma_m^{\sim})_k^2}}, \quad (8)$$

where  $k$  refers to the model parameter index,  $V_k$  is the volume of voxel  $k$ ,  $\mathcal{P}$  is the set of model parameters considered for the analysis, and  $\sigma_m^{\sim}$  refers to the model uncertainty estimate.

If the data uncertainty is well-estimated, then  $\xi_m^2 = 1$ . As an experiment, we add random noise with a known distribution to the analytical data (i.e. to those obtained using  $\mathbf{d}^{\text{analytical}} = \mathbf{Gm}^{\text{input}}$ ). In this case, the simulated data uncertainty is perfectly known and we obtain exactly  $\xi_m^2 = 1$ . In the case of our synthetic tomography with phase delays measured on SEM waveforms, we obtain  $\xi_m^2 \approx 33 \gg 1$  when we only consider the propagation of data measurement uncertainty into model measurement uncertainty. This model uncertainty estimate is dramatically under-estimated as we may have underestimated the data measurement uncertainty and/or lack the theoretical uncertainty. We thus need to either upscale or add another component to the model uncertainty to account for this. We can write:

$$\sigma_{m(k)}^{\text{total}^2} = \alpha^2 \sigma_{m(k)}^{\text{measurement}^2} + \beta^2. \quad (9)$$

Here,  $\alpha$  is the factor needed to upscale the model measurement uncertainty to account for the fact the measurement uncertainty itself might be underestimated.  $\beta$  is the theoretical uncertainty term that appears as an added component. We can now vary  $\alpha$  and  $\beta$  independently and investigate for which combinations we obtain  $\xi_m^2 = 1$ . Note that in this analysis the scaling factor  $\alpha$  and the added uncertainty component  $\beta$  are both assumed to be constant over all model parameters involved (consisting here of all model parameters for  $V_{SV}$  at 112 km depth).

Figure 9 shows the evolution of  $\xi_m^2$  for various combinations of  $\alpha$  and  $\beta$ . We use this plot to illustrate three distinct cases. (i) The model measurement uncertainty serves as total model uncertainty, i.e. no upscaling nor added component, i.e.  $\alpha = 1$  and  $\beta = 0$ . In this case,  $\xi_m^2 \approx 33$  falls in the under-estimated uncertainty region. (ii) We only upscale the model measurement uncertainty to obtain  $\xi_m^2 = 1$ , with  $\beta = 0$ , which requires  $\alpha \approx 5.74$ . (iii) We add an uncertainty component without upscaling the model measurement uncertainty to obtain  $\xi_m^2 = 1$ , with  $\alpha = 1$ , which requires  $\beta \approx 0.49$ . This shows that the model measurement uncertainty explains only a small part of the discrepancy between the filtered input and the model solution. For comparison, the mean measurement model uncertainty is 0.09 (without upscaling). This means that the theoretical model uncertainty that needs to be added to the measurement uncertainty for a correct total model uncertainty is  $0.49/0.09 \approx 5.5$  times the model measurement uncertainty (without any upscaling). Therefore, in this case, the total model uncertainty is dominated by what we refer to as theoretical uncertainty. In other words, the uncertainty provided by the measurement algorithm explains only a small fraction of the total magnitude of the uncertainty.

## 6 Discussion

The SOLA-finite-frequency framework for surface-wave tomography we present in this study makes it possible to obtain 3D resolution and uncertainty estimates in surface-wave tomography. Here, we discuss our findings regarding resolution and uncertainty in more detail and discuss possible future directions.

### 6.1 Full 3D resolution

While our setup does not handle non-linearity, it offers many advantages related to the seismic model resolution: we obtain the full resolution matrix in a computationally efficient way; the resolution is fully 3D; it is unbiased by construction (local averaging weights sum to 1) as demonstrated by Zanolli et al. (2017); and we have to some extent direct control over the resolution we obtain by choosing the target kernels. This is in contrast with most other studies that typically have assessed the resolution through inverting synthetic input models (e.g. French et al., 2013), checkerboard tests (e.g. Zhou et al., 2006; Auer et al., 2014; Rawlinson and Spakman, 2016), point spread functions (Ritsema et al., 2004; Bonadio et al., 2021), using the Hessian in the context of full-waveform inversion (e.g. Fichtner and Trampert, 2011), statistical methods using Monte Carlo approaches or transdimensional tomography (e.g. An, 2012; Bodin et al., 2012b; Sambridge et al., 2013), or other algebraic manipulations (e.g. Fichtner and Zunino, 2019; Shapiro et al., 2005; French and Romanowicz, 2014). Since surface-wave tomography is often based on a two-step approach, estimates for the resolution have typically been only 2D (lateral) or 1D (vertical), but there are some recent examples of 3D applica-

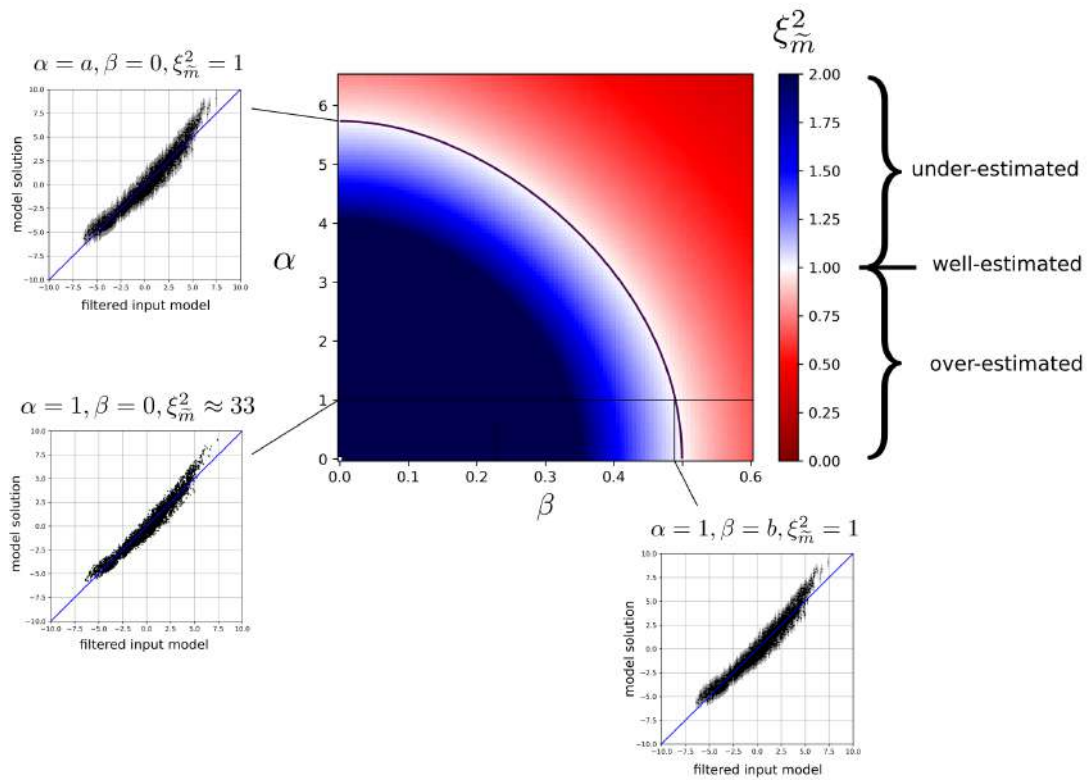


**Figure 9** Model uncertainty analysis. The central plot shows the value of  $\xi_m^2$  (the misfit between the model solution and the filtered input model, normalised by the model uncertainty) for various combinations of the scaling factor  $\alpha$  and added theoretical component  $\beta$ . In general, one should aim to find values of  $\alpha$  and  $\beta$  that lead to  $\xi_m^2 = 1$  (the black line in the white area). For small values of both  $\alpha$  and  $\beta$  (blue region, or lower-left part of the plot),  $\xi_m^2 > 1$ , meaning that the model uncertainty is under-estimated, while the red regions indicate the model uncertainty is overestimated. The three cross-plots show the velocity variations in the model solution versus those in the filtered input model for three cases: (i) upscaled measurement uncertainty and no added component (upper-left), (ii) no upscaling nor added component (lower-left), and (iii) an added component, but no upscaling (lower-right). Note that only the error bars representing the total model uncertainty for various combinations of  $\alpha$  and  $\beta$  change between these plots.

tions, for example using transdimensional tomography (Zhang et al., 2018, 2020)

In this synthetic study, we find that the resolution is laterally good enough to qualitatively retrieve the main features of the input model (compare Figure 8a and b). These large-scale or strong anomalies are features most surface-wave tomography models agree on. This may be surprising given the small number of data in our inversion (47 700). We believe there are three main reasons for this: (i) we carefully select our input data; (ii) finite-frequency theory provides improved constraints compared to ray theory since one 3D sensitivity kernel constrains more model parameters than a thin ray, while also being more accurate (e.g. Zhou et al., 2005); and (iii) the SOLA inversion performs well in optimally using the data sensitivities. Point (ii) shares some similarities with adjoint methods used in full waveform inversion, given the volumetric nature of the adjoint sensitivity kernels (e.g. Monteiller et al., 2015).

The SOLA method consists of individual inversions for each model parameter without imposing any global constraint on all model parameters together. Therefore, the fact that we recover large-scale structures in the filtered model and model solution that are consistent with the input model is encouraging (Zaroli, 2016). The

global consistency of the model is provided indirectly by the overlap between the averaging kernels. However, compared to the input model, some short-scale variability arises in the filtered input, where adjacent cells show relatively strong differences. This is due to the point-wise nature of the SOLA inversion, combined with the absence of a smoothness criterion, and the smooth nature of the input model itself. Using a coarser target resolution would produce a smoother model, but would also filter out heterogeneities that are informative. Even though we present our results by plotting the mean of our model parameters in adjacent voxels (to visualise them as a tomographic model), it is important to remember that these are local average estimates.

In the above, we typically assess the performance of the resolution by comparing the filtered model to the input model. In doing this, we must keep in mind that our ability to retrieve the input model depends on the roughness of the input model itself. In particular, if the input model had contained shorter scale structure, we might not have been able to resolve it. While the resolution itself remains reliable, the comparison of input *versus* output models depends on the input itself; this bears some similarity with the inherent limitations of checkerboard tests (e.g. L  v  que et al., 1993; Rawlinson

and Spakman, 2016). The full resolution itself remains necessary for robust model interpretations.

Since the data sensitivity and the resolution are fully 3D, we can confidently interpret the model resolution and uncertainty at all depths. This is a great advantage compared to our earlier 2D work (Latallier et al., 2022), where the data sensitivity was imposed based on the lateral ray coverage (assuming ray theory). As a consequence, this study was likely too optimistic about the resolution at greater depth and therefore it was not possible to clearly state up to what depth the resolution and uncertainty estimates could be robustly interpreted. Moreover, since our resolution is fully 3D, we can investigate vertical resolution effects here. In addition to the well-known lateral smearing that arises in surface-wave tomography (discussed by Latallier et al. (2022)), our averaging kernels indicate also significant vertical smearing (or depth leakage) in the cross-sections (Figures 3 and 4). Similar observations have been made in the context of full waveform inversion through assessment of the Hessian (e.g. Fichtner and Trampert, 2011). For some model parameters, the averages we recover relate primarily to structure above or below the ‘true’ location as the averaging kernel is shifted upward or downward relative to the target kernel. In particular, the structure obtained at greater depth tends to be an average over shallower structure, with the effect becoming stronger with depth. Ignoring this full 3D resolution could thus lead to biased interpretations of surface-wave tomography, for example in studies of the age-depth trends of the oceanic lithosphere (e.g. Ritzwoller et al., 2004; Priestley and McKenzie, 2006; Maggi et al., 2006b; Isse et al., 2019). This synthetic study thus emphasises the importance of taking vertical resolution into account when interpreting surface-wave tomography models and provides a quantitative way to estimate the depth to which a surface-wave tomography model should be interpreted. Within the SOLA approach, the depth leakage could potentially be reduced by varying the trade-off parameter with depth, and by adding a directionality to the trade-off parameter. We could also use a full covariance matrix or include a weighting matrix in the optimisation problem of Equation 5, to give more weight to low frequency data (which would improve the resolution at greater depth).

Resolution and uncertainty are closely related: regions with high resolution tend to have high uncertainty, and *vice versa*. In this study, we find that the propagation of uncertainty decreases with depth (Fig. 5). This might be counter-intuitive as we expect the sensitivity of surface waves to decrease with depth. However, this observation has also been noted in other studies (e.g. Zhang et al., 2018; Earp et al., 2020; Latallier et al., 2022). Our 3D resolution provides a robust explanation for the decrease of uncertainty with depth. As depth increases, the resolution typically degrades, in the sense that it does not represent the average focused around the target location. It rather tends to represent an average over regions with high data sensitivity (averages are estimated over larger volumes and are shifted spatially with respect to their associated target location), leading to lower uncertainties. This illus-

trates that a combined analysis of uncertainty and 3D resolution is necessary to fully understand the limitations of surface-wave tomographic models.

## 6.2 Robust uncertainty estimates?

In this study, we estimate model uncertainty by propagating data uncertainty into model uncertainty using SOLA, which works for linear(ised) inverse problems. Other studies have used Bayesian approaches (e.g. Bodin et al., 2012b; Sambridge et al., 2013; Zhang et al., 2018), recently helped by machine learning approaches (e.g. Earp et al., 2020), where the posterior probability density function for the model can be interpreted as a measure of uncertainty. The Hessian has also been used in full waveform inversions (e.g. Fichtner and Trampert, 2011). However, in non-linear problems, the interpretation becomes more difficult. In general, we are left with the problem of estimating robust data uncertainties, which in the Bayesian philosophy entails finding the right prior probability distribution (though in this case non-informative priors could be used or compared with the posteriors).

We have estimated the measurement uncertainty with repeated sampling, changing the time window using the multi-taper technique. This is not dissimilar to previous studies, which have used summary rays, bootstrapping or perturbation methods to estimate the data mean and measurement uncertainty (e.g. Maggi et al., 2006b; Amiri et al., 2023; Asplet et al., 2020). Summary rays are not useful in our case as the sensitivity kernels depend on source mechanisms. However, future studies could compare the uncertainty we obtain with the multitaper technique to estimates using bootstrapping. Bootstrapping could also provide a range of subdatasets with differing levels of uncertainty that could be used to investigate the effect on the model solution using SOLA. This would however have a significant computational cost.

In general, model uncertainty appears to be underestimated. This is clear from meta-analyses of published tomography models that show that the discrepancies are stronger than the typical error bars (e.g. Hosseini et al., 2018; Marignier et al., 2020; De Viron et al., 2021). This has led authors to use simple *ad hoc* criteria for upscaling the measurement uncertainty. For example, Latallier et al. (2022) use a least-squares  $\chi$ -test to upscale the uncertainty by a factor up to 3.4, while Lin et al. (2009) multiply their random error uncertainty estimates by 1.5 to obtain a more realistic model uncertainty estimate. While the measurement uncertainty might indeed be underestimated (which led us to define the factor  $\alpha$  in section 5.2), the total uncertainty also needs to account for additional theoretical uncertainty (the factor  $\beta$  in section 5.2). Theoretical errors are technically deterministic, but for mathematical convenience we have treated them as random variables.

Theoretical uncertainty has typically been estimated using Monte-Carlo approaches in synthetic tests, during which input parameters are varied and the range of recovered data values is recorded as uncertainty. For example, for surface-wave dispersion measurements,



Bozdağ and Trampert (2008) investigated the theoretical errors induced by imperfect crustal corrections, while Amiri et al. (2023) estimated the theoretical error induced by source mislocation. Similarly, Akbarashrafi et al. (2018) investigated the theoretical error produced by different coupling approximations on normal mode measurements, finding that reported data uncertainties need to be at least doubled to account for the errors due to theoretical omissions. In this work, we instead estimated the effect of the theoretical uncertainties on the model using a synthetic tomography setup that included many sources of theoretical uncertainty simultaneously. The effect of resolution was removed by filtering the input model so that discrepancies between our model estimate and the filtered input model represent the total uncertainty. After propagating the data measurement uncertainty into model measurement uncertainty, we noticed that these need to be upscaled by  $\sim 5.5$  to obtain a  $\xi^2$  of 1. This means that the theoretical model uncertainty is  $\sim 5.5$  times larger than the model measurement uncertainty, assuming that the data measurement uncertainty is estimated correctly. The theoretical model uncertainty is thus larger than previously proposed factors of 1.5–3.4 (Lin et al., 2009; Latalerie et al., 2022), providing further evidence that the model uncertainty is indeed severely underestimated if we only propagate the data measurement uncertainty. Whether there is a need to upscale the measurement uncertainty naturally also depends on the specifics of the study and on the reliability of the measurement uncertainty estimate itself.

The main aim of this study is to provide a framework for surface-wave tomography with robust model statistics, including both the 3D resolution and total uncertainty. However, we still suffer from several drawbacks. For instance, although our measurement uncertainty should account for contamination by other phases or higher modes and cycle skipping, visual inspection indicates that this is not always the case (Figure 6). In the case of poor measurements (e.g. due to a missed cycle skip) with low uncertainty, we underestimate the measurement uncertainty and consequently overestimate the theoretical uncertainty. This is the rationale behind the factor  $\alpha$  to upscale the measurement uncertainty in Section 5.2 and illustrates the difficulty of correctly estimating the measurement uncertainty. An interesting alternative approach was presented by several studies (Bodin and Sambridge, 2009; Bodin et al., 2012a; Zhang et al., 2020; Del Piccolo et al., 2024), which use a hierarchical transdimensional Bayesian approach where the data uncertainty is an output of the inverse process itself, rather than an input.

Another drawback of our approach is that our estimates of theoretical uncertainty depend on the input model used, i.e. S362ANI (Kustowski et al., 2008). The validity of the forward theory depends on several assumptions (e.g. forward scattering, paraxial approximation) whose applicability depends on the properties of the medium in which waves propagate (e.g. Liu and Zhou, 2013; Parisi et al., 2015). It is therefore important to perform our analysis in an Earth-like model and further work could investigate the dependency on

the input model. Additionally, the scaling factor  $\alpha$  (up-scaling of the measurement uncertainty) and the added component  $\beta$  (representing the theoretical uncertainty) need to be determined for a sufficiently large number of model parameters for the results to be statistically significant (here we considered all model parameters at 112 km depth). In particular, we would recommend to determine these parameters for each depth in the model independently, as velocity structure and the magnitudes of measurement and theoretical uncertainties likely change with depth.

Furthermore, the theoretical model uncertainty is estimated in the model space, and therefore may depend in a non-trivial way on the model resolution. This would be reflected by a dependency of  $\xi^2$  on the model resolution. This means that while the theoretical model uncertainty is accurately estimated for this particular solution, it may not apply to another inverse solution with a different resolution. One way to obtain the theoretical model uncertainty for models with different resolution without having to repeat their estimation in the same way, could be to compute the contribution of theoretical uncertainty on the data themselves using the sensitivity matrix, and then to propagate this contribution for models with different resolution using their respective generalised inverse matrices.

We further assume the data uncertainties to be uncorrelated, whereas in reality we expect them to be correlated to some extent – e.g. an error in the source location or mechanism will impact several measurements. In theory, it is possible to account for correlations between data uncertainties, but estimating these correlations remains a challenge in surface-wave tomography. The addition of the theoretical uncertainty contribution to measurement uncertainty relies on the assumption that they are normally distributed. Furthermore, the assumption of a zero-mean Gaussian distribution for the data errors seems reasonable, but the use of more general probability distributions could also be investigated (e.g. Tarantola, 2005). Note that the off-diagonal terms of the model covariance matrix are also non-zero (even with a diagonal data covariance matrix). In SOLA we do not consider them explicitly because the information they carry is already embedded in the resolution.

Lastly, we estimate the theoretical uncertainty from the discrepancy between the filtered input model and the model solution based on measurements on SEM seismograms. Since the crustal model we assume for the crustal corrections is exactly the same as in the input model, and the source parameters used for generating the reference seismograms are exactly the same as for the SEM seismograms, there is no theoretical error associated with errors in the crustal model or source solution in our synthetic framework. Nevertheless, these two components likely introduce non-negligible errors in reality (e.g. Marone and Romanowicz, 2007; Bozdağ and Trampert, 2008; Panning et al., 2010; Ferreira et al., 2010; Liu and Zhou, 2013; Latalerie, 2022; Amiri et al., 2023). Additionally, we base our kernels on the reference model *stw105*, which is already optimal for the input model S362ANI that we aim to retrieve. This inherently limits the magnitude of theoretical errors arising

due to non-linearity in this study. Additionally, non-linearities are expected to be stronger in the real Earth than in the relatively smooth input model S362ANI. In future, additional work could be done to estimate the model uncertainty related to these components, which could be incorporated in the proposed theoretical uncertainty estimate. In addition, we use spectral element modelling (SEM) to provide the ground truth, but any deviation from SEM in reality would lead to additional theoretical errors in a data-based study.

The restriction of SOLA inversion to linear problems remains an important overall drawback of the method. Here we treat non-linearity as an additional component in the uncertainty. Accounting for non-linearities with iterative inversion schemes can improve the models significantly (e.g. Thrastarson et al., 2024; Rodgers et al., 2024) and would allow for a better representation of the crust (e.g. Marone and Romanowicz, 2007; Bozdağ and Trampert, 2008; Panning et al., 2010; Liu and Zhou, 2013; Chen and Romanowicz, 2024). However, non-linearities would also make the computation and interpretation of the resolution and uncertainty more complicated. The extension of Backus-Gilbert theory to non-linear inverse problems as proposed by Snieder (1991) could help to better account for non-linearities with SOLA and should be the subject of future work.

Despite the drawbacks outlined above, we believe that our study provides a valuable starting point to obtain 3D resolution and to estimate theoretical model uncertainty in surface-wave tomography, upon which future work can build. This information is vital for robust model interpretations and to reconcile existing discrepancies between published tomography models (e.g. Hosseini et al., 2018; Marignier et al., 2020; De Viron et al., 2021).

### 6.3 Future directions

The depth sensitivity and thus resolution in this study is limited by the restriction to fundamental-mode surface-wave data. This can be mitigated by adding measurements for surface-wave overtones. In theory, including these in the presented framework is trivial, but it will be important to carefully estimate the data uncertainty for these new measurements. The resolution and uncertainty produced in our setup can be used to inform other tomographic studies. Our 3D resolution maps indicate how well certain model parameters are constrained depending on their position and particularly with depth. Based on this, we may choose sets of source-receiver paths and frequencies that best suit a certain target. For example, to better homogenise the resolution with depth, we may want to increase the number and/or the relative weight of low frequency data.

The obvious next step is to apply the approach presented here to real data, using the lessons learned in this synthetic study. As noted here, the depth leakage at depths greater than  $\sim 100$  km becomes extremely strong for a dataset that is restricted to the fundamental mode. This suggests that including overtones will be necessary to obtain a model that is well-resolved deeper down in the mantle. In general, the information on 3D reso-

lution and uncertainty obtained using SOLA would be particularly useful for testing geodynamic predictions (Freissler et al., 2022). In addition, this information would ensure that we only interpret the tomographic models to their limits, and not beyond, being aware of potential resolution artefacts, especially with depth.

There are many other directions for further development. For example, it is possible to extend the SOLA-finite-frequency framework for surface-wave tomography to other data and physical parameters, e.g. amplitude measurements to study anelasticity in the upper-mantle (e.g. Zhou, 2009b). These could be investigated independently, or through a joint approach, thus reducing theoretical uncertainty due to neglecting the effect of other physical parameters.

## Conclusion

In this contribution, we have combined the Backus-Gilbert-based SOLA inverse method with finite-frequency theory in a synthetic study of the Pacific upper mantle. Our 3D modelling and inversion framework enables us to control and produce uncertainty and resolution information together with the surface-wave tomography model. We have used a synthetic framework to demonstrate the reliability of our approach and to investigate the effect of 3D resolution, laterally and vertically, in surface-wave tomography. We find that the limited resolution induces well-known artefacts, including lateral smearing effects where data coverage is poor or highly anisotropic. More importantly, we show that limited vertical resolution can induce strong artefacts with model parameters potentially representing averages of ‘true’ Earth properties at much shallower depth. Knowledge of this full 3D resolution is crucial for robust interpretations of surface-wave tomography models. Our synthetic setup allows us to also explore the reliability of model uncertainty estimates. We find that the theoretical uncertainty, required to match the filtered input model, might be much larger than the measurement uncertainty in the data. This demonstrates the need to account for both measurement and theoretical uncertainty in surface-wave tomography. We believe that our study is a starting point towards better use and interpretation of surface-wave tomography models.

## Acknowledgments

The authors are grateful to the editor, Chiara Civiero, and to Andreas Fichtner and an anonymous reviewer whose detailed comments have helped to improve this manuscript. This research is supported by the UKRI NERC Large grant “Mantle Circulation Constrained (MC2): A multidisciplinary 4D Earth framework for understanding mantle upwellings” (NE/T01248X/1). PK acknowledges financial support from a Royal Society University Research Fellowship (URF \1 \180377). CZ acknowledges financial support from ITES (Institut Terre et Environnement de Strasbourg, UMR 7063) for a research visit to Oxford. This study used the

ARCHER2 UK National Supercomputing Service (<https://www.archer2.ac.uk>). For this study we made extensive use of GNU/Linux and Python (including packages Scipy, Numpy, Matplotlib, Pandas and Multiprocessing). For the purpose of open access, the authors have applied a CC BY public copyright license to any Author Accepted Manuscript version arising.

## Data and code availability

Seismic source solutions were downloaded from the Global Centroid Moment Tensor (GCMT) Catalog (Dziewonski et al., 1981; Ekström et al., 2012). The facilities of the EarthScope Consortium were used to access waveforms and related metadata and derived data products. These services are funded through the National Science Foundation's Seismological Facility for the Advancement of Geoscience (SAGE) Award under Cooperative Agreement EAR-1724509. All waveforms used in this study are SEM synthetics from the GlobalShakeMovie project (Tromp et al., 2010), and were obtained through IRIS DMC (Hutko et al., 2017; IRIS DMC, 2012). To compute the finite-frequency sensitivity kernels, we used software provided by Ying Zhou (Zhou, 2009b), available via their webpage. To compute the reference seismograms in a 1D radial Earth model using normal modes summation, we used MINEOS 1.0.2 (Masters et al., 2011) published under the GPL2 license. We thank the Computational Infrastructure for Geodynamics (<http://geodynamics.org>), which is funded by the National Science Foundation under awards EAR-0949446, EAR-1550901, and EAR-2149126 for making the code available.

The SOLA tomography code used in this study consists of running the LSQR algorithm of Paige and Saunders (1982) with specific input matrices and vectors. These inputs can be constructed from the sensitivity matrix and target kernels as detailed in Appendix A1 of Zaroli (2016). The LSQR code is freely downloadable from the webpage of the Systems Optimisation Laboratory (Stanford University): <https://web.stanford.edu/group/SOL/software/lqr/>. A pre-constructed software package for SOLA tomography is available from Christophe Zaroli (c.zaroli@unistra.fr) upon e-mail request.

## References

- Akbarashrafi, F., Al-Attar, D., Deuss, A., Trampert, J., and Valentine, A. P. Exact free oscillation spectra, splitting functions and the resolvability of Earth's density structure. *Geophysical Journal International*, 213(1):58–76, Apr. 2018. doi: 10.1093/gji/ggx539.
- Amiri, S., Maggi, A., Tatar, M., Zigone, D., and Zaroli, C. Rayleigh wave group velocities in North-West Iran: SOLA Backus-Gilbert vs. Fast Marching tomographic methods. *Seismica*, 2(2), Dec. 2023. doi: 10.26443/seismica.v2i2.1011.
- An, M. A simple method for determining the spatial resolution of a general inverse problem. *Geophysical Journal International*, 191(2):849–864, Nov. 2012. doi: 10.1111/j.1365-246X.2012.05661.x.
- Asplet, J., Wookey, J., and Kendall, M. A potential post-perovskite province in D" beneath the Eastern Pacific: evidence from new analysis of discrepant SKS–SKKS shear-wave splitting. *Geophysical Journal International*, 221(3):2075–2090, June 2020. doi: 10.1093/gji/ggaa114.
- Auer, L., Boschi, L., Becker, T. W., Nissen-Meyer, T., and Giardini, D. Savani : A variable resolution whole-mantle model of anisotropic shear velocity variations based on multiple data sets. *Journal of Geophysical Research: Solid Earth*, 119(4):3006–3034, Apr. 2014. doi: 10.1002/2013JB010773.
- Backus, G. and Gilbert, F. The Resolving Power of Gross Earth Data. *Geophysical Journal International*, 16(2):169–205, Oct. 1968. doi: 10.1111/j.1365-246X.1968.tb00216.x.
- Backus, G. E. and Gilbert, F. Uniqueness in the inversion of inaccurate gross Earth data. *Philosophical Transactions of the Royal Society of London. Series A, Mathematical and Physical Sciences*, 266(1173):74, 1970. doi: 10.1098/rsta.1970.0005.
- Backus, G. E. and Gilbert, J. F. Numerical Applications of a Formalism for Geophysical Inverse Problems. *Geophysical Journal International*, 13(1-3):247–276, July 1967. doi: 10.1111/j.1365-246X.1967.tb02159.x.
- Barmin, M. P., Ritzwoller, M. H., and Levshin, A. L. A Fast and Reliable Method for Surface Wave Tomography. *Pure and Applied Geophysics*, 158:25, 2001. doi: 10.1007/PL00001225.
- Bassin, C., Laske, G., and Masters, G. The Current Limits of Resolution for Surface Wave Tomography in North America. *Eos, Transactions American Geophysical Union*, 81(F897), 2000.
- Boaga, J., Vignoli, G., and Cassiani, G. Shear wave profiles from surface wave inversion: the impact of uncertainty on seismic site response analysis. *Journal of Geophysics and Engineering*, 8(2):162–174, June 2011. doi: 10.1088/1742-2132/8/2/004.
- Boaga, J., Vignoli, G., and Cassiani, G. Reply to comment on 'Shear wave profile from surface wave inversion: the impact of uncertainty on seismic site response analysis'. *Journal of Geophysics and Engineering*, 9(2):244–246, Apr. 2012. doi: 10.1088/1742-2132/9/2/244.
- Bodin, T. and Sambridge, M. Seismic tomography with the reversible jump algorithm. *Geophysical Journal International*, 178(3):1411–1436, Sept. 2009. doi: 10.1111/j.1365-246X.2009.04226.x.
- Bodin, T., Sambridge, M., Rawlinson, N., and Arroucau, P. Trans-dimensional tomography with unknown data noise. *Geophysical Journal International*, 189(3):1536–1556, June 2012a. doi: 10.1111/j.1365-246X.2012.05414.x.
- Bodin, T., Sambridge, M., Tkalčić, H., Arroucau, P., Gallagher, K., and Rawlinson, N. Transdimensional inversion of receiver functions and surface wave dispersion: TRANSDIMENSIONAL INVERSION OF RF AND SWD. *Journal of Geophysical Research: Solid Earth*, 117(B2):n/a–n/a, Feb. 2012b. doi: 10.1029/2011JB008560.
- Bonadio, R., Lebedev, S., Meier, T., Arroucau, P., Schaeffer, A. J., Licciardi, A., Agius, M. R., Horan, C., Collins, L., O'Reilly, B. M., Readman, P. W., and Ireland Array Working Group. Optimal resolution tomography with error tracking and the structure of the crust and upper mantle beneath Ireland and Britain. *Geophysical Journal International*, 226(3):2158–2188, June 2021. doi: 10.1093/gji/ggab169.
- Bozdağ, E. and Trampert, J. On crustal corrections in surface wave tomography. *Geophysical Journal International*, 172(3):1066–1082, Mar. 2008. doi: 10.1111/j.1365-246X.2007.03690.x.
- Chen, L.-W. and Romanowicz, B. On accounting for the effects of crust and uppermost mantle structure in global scale full-waveform inversion. *Geophysical Journal International*, 239(1):662–674, 2024. doi: 10.1093/gji/ggae282.
- Dahlen, F. A. and Tromp, J. *Theoretical Global Seismology*. Princeton



- ton University Press, Dec. 1999. doi: 10.1515/9780691216157.
- Dahlen, F. A., Hung, S.-H., and Nolet, G. Fréchet kernels for finite-frequency traveltimes-I. Theory. *Geophysical Journal International*, 141(1):157–174, Apr. 2000. doi: 10.1046/j.1365-246X.2000.00070.x.
- De Viron, O., Van Camp, M., Grabkowiak, A., and Ferreira, A. M. G. Comparing global seismic tomography models using varimax principal component analysis. *Solid Earth*, 12(7):1601–1634, July 2021. doi: 10.5194/se-12-1601-2021.
- Debayle, E. SV-wave azimuthal anisotropy in the Australian upper mantle: preliminary results from automated Rayleigh waveform inversion. *Geophysical Journal International*, 137(3): 747–754, June 1999. doi: 10.1046/j.1365-246x.1999.00832.x.
- Debayle, E. and Kennett, B. L. N. The Australian continental upper mantle: Structure and deformation inferred from surface waves. *Journal of Geophysical Research: Solid Earth*, 105(B11): 25423–25450, Nov. 2000. doi: 10.1029/2000JB900212.
- Debayle, E. and Lévêque, J. J. Upper mantle heterogeneities in the Indian Ocean from waveform inversion. *Geophysical Research Letters*, 24(3):245–248, Feb. 1997. doi: 10.1029/96GL03954.
- Debayle, E. and Sambridge, M. Inversion of massive surface wave data sets: Model construction and resolution assessment. *Journal of Geophysical Research: Solid Earth*, 109(B2), Feb. 2004. doi: 10.1029/2003JB002652.
- Del Piccolo, G., VanderBeek, B. P., Faccenda, M., Morelli, A., and Byrnes, J. S. Imaging Upper-Mantle Anisotropy with Transdimensional Bayesian Monte Carlo Sampling. *Bulletin of the Seismological Society of America*, 114(3):1214–1226, June 2024. doi: 10.1785/0120230233.
- Dziewonski, A. M., Chou, T.-A., and Woodhouse, J. H. Determination of earthquake source parameters from waveform data for studies of global and regional seismicity. *Journal of Geophysical Research: Solid Earth*, 86(B4):2825–2852, Apr. 1981. doi: 10.1029/JB086iB04p02825.
- Earp, S., Curtis, A., Zhang, X., and Hansteen, F. Probabilistic neural network tomography across Grane field (North Sea) from surface wave dispersion data. *Geophysical Journal International*, 223(3):1741–1757, Oct. 2020. doi: 10.1093/gji/ggaa328.
- Ekström, G. A global model of Love and Rayleigh surface wave dispersion and anisotropy, 25–250 s: Global dispersion model GDM52. *Geophysical Journal International*, 187(3):1668–1686, Dec. 2011. doi: 10.1111/j.1365-246X.2011.05225.x.
- Ekström, G., Tromp, J., and Larson, E. W. F. Measurements and global models of surface wave propagation. *Journal of Geophysical Research: Solid Earth*, 102(B4):8137–8157, Apr. 1997. doi: 10.1029/96JB03729.
- Ekström, G., Nettles, M., and Dziewoński, A. The global CMT project 2004–2010: Centroid-moment tensors for 13,017 earthquakes. *Physics of the Earth and Planetary Interiors*, 200–201:1–9, June 2012. doi: 10.1016/j.pepi.2012.04.002.
- Ferreira, A. M. G., Woodhouse, J. H., Visser, K., and Trampert, J. On the robustness of global radially anisotropic surface wave tomography. *Journal of Geophysical Research: Solid Earth*, 115 (B4):2009JB006716, Apr. 2010. doi: 10.1029/2009JB006716.
- Fichtner, A. and Trampert, J. Resolution analysis in full waveform inversion: Resolution in full waveform inversion. *Geophysical Journal International*, 187(3):1604–1624, Dec. 2011. doi: 10.1111/j.1365-246X.2011.05218.x.
- Fichtner, A. and Zunino, A. Hamiltonian Nullspace Shuttles. *Geophysical Research Letters*, 46(2):644–651, Jan. 2019. doi: 10.1029/2018GL080931.
- Foulger, G. R., Panza, G. F., Artemieva, I. M., Bastow, I. D., Cammarano, F., Evans, J. R., Hamilton, W. B., Julian, B. R., Lustrino, M., Thybo, H., and Yanovskaya, T. B. Caveats on tomographic images. *Terra Nova*, 25(4):259–281, Aug. 2013. doi: 10.1111/ter.12041.
- Freissler, R., Zaroli, C., Lambotte, S., and Schuberth, B. S. A. Tomographic filtering via the generalized inverse: a way to account for seismic data uncertainty. *Geophysical Journal International*, 223(1):254–269, Oct. 2020. doi: 10.1093/gji/ggaa231.
- Freissler, R., Schuberth, B. S., and Zaroli, C. The relevance of full 3D-wavefield simulations for the tomographic filtering of geodynamic models, Mar. 2022. doi: 10.5194/egusphere-egu22-11686.
- Freissler, R., Schuberth, B. S. A., and Zaroli, C. A concept for the global assessment of tomographic resolution and uncertainty. *Geophysical Journal International*, page ggaa178, May 2024. doi: 10.1093/gji/ggae178.
- French, S., Lekic, V., and Romanowicz, B. Waveform Tomography Reveals Channelled Flow at the Base of the Oceanic Asthenosphere. *Science*, 342(6155):227–230, Oct. 2013. doi: 10.1126/science.1241514.
- French, S. W. and Romanowicz, B. A. Whole-mantle radially anisotropic shear velocity structure from spectral-element waveform tomography. *Geophysical Journal International*, 199 (3):1303–1327, Dec. 2014. doi: 10.1093/gji/ggu334.
- Greenfield, T., Gilligan, T., Pilia, S., Cornwell, D. G., Tongkul, F., Widiyantoro, S., and Rawlinson, N. Post-Subduction Tectonics of Sabah, Northern Borneo, Inferred From Surface Wave Tomography. *Geophysical Research Letters*, 49(3), Feb. 2022. doi: 10.1029/2021GL096117.
- Hjörleifsdóttir, V. *Earthquake Source Characterization Using 3D Numerical Modeling*. PhD thesis, California Institute of Technology, Apr. 2007. doi: 10.7907/M17S-7W40. Medium: PDF Version Number: Final.
- Hosseini, K., Matthews, K. J., Sigloch, K., Shephard, G. E., Domeier, M., and Tsekhmistrenko, M. SubMachine: Web-Based Tools for Exploring Seismic Tomography and Other Models of Earth's Deep Interior. *Geochemistry, Geophysics, Geosystems*, 19(5): 1464–1483, May 2018. doi: 10.1029/2018GC007431.
- Hutko, A. R., Bahavar, M., Trabant, C., Weekly, R. T., Fossen, M. V., and Ahern, T. Data Products at the IRIS-DMC: Growth and Usage. *Seismological Research Letters*, 88(3):892–903, May 2017. doi: 10.1785/0220160190.
- IRIS DMC. Data Services Products: ShakeMovieSynthetics 1D & 3D synthetic seismograms from the Global ShakeMovie project, 2012. doi: 10.17611/DP/SYN.1.
- Isse, T., Kawakatsu, H., Yoshizawa, K., Takeo, A., Shiobara, H., Sugioka, H., Ito, A., Suetsugu, D., and Reymond, D. Surface wave tomography for the Pacific Ocean incorporating seafloor seismic observations and plate thermal evolution. *Earth and Planetary Science Letters*, 510:116–130, Mar. 2019. doi: 10.1016/j.epsl.2018.12.033.
- Komatitsch, D. and Tromp, J. Spectral-element simulations of global seismic wave propagation-II. Three-dimensional models, oceans, rotation and self-gravitation. *Geophysical Journal International*, 150(1):303–318, July 2002. doi: 10.1046/j.1365-246X.2002.01716.x.
- Komatitsch, D. and Vilotte, J.-P. The spectral element method: An efficient tool to simulate the seismic response of 2D and 3D geological structures. *Bulletin of the Seismological Society of America*, 88(2):368–392, Apr. 1998. doi: 10.1785/BSSA0880020368.
- Kustowski, B., Ekström, G., and Dziewoński, A. M. Anisotropic shear-wave velocity structure of the Earth's mantle: A global model. *Journal of Geophysical Research*, 113(B6):B06306, June 2008. doi: 10.1029/2007JB005169.

- Laske, G. and Masters, G. Constraints on global phase velocity maps from long-period polarization data. *Journal of Geophysical Research: Solid Earth*, 101(B7):16059–16075, July 1996. doi: 10.1029/96JB00526.
- Laske, G., Masters, G., and Zürn, W. Frequency-dependent polarization measurements of long-period surface waves and their implications for global phase-velocity maps. *Physics of the Earth and Planetary Interiors*, 84(1-4):111–137, July 1994. doi: 10.1016/0031-9201(94)90037-X.
- Latallier, F. *Seismic tomography of plume-like upwellings in the French Polynesia region using Backus-Gilbert inversion*. Theses, Université de Strasbourg, Dec. 2022. <https://theses.hal.science/tel-04193813>. Issue: 2022STRAH012.
- Latallier, F., Zaroli, C., Lambotte, S., and Maggi, A. Analysis of tomographic models using resolution and uncertainties: a surface wave example from the Pacific. *Geophysical Journal International*, 230(2):893–907, Apr. 2022. doi: 10.1093/gji/ggac095.
- Lebedev, S. and Nolet, G. Upper mantle beneath Southeast Asia from S velocity tomography: UPPER MANTLE BENEATH SE ASIA. *Journal of Geophysical Research: Solid Earth*, 108(B1), Jan. 2003. doi: 10.1029/2000JB000073.
- Lin, F.-C., Ritzwoller, M. H., and Snieder, R. Eikonal tomography: surface wave tomography by phase front tracking across a regional broad-band seismic array. *Geophysical Journal International*, 177(3):1091–1110, June 2009. doi: 10.1111/j.1365-246X.2009.04105.x.
- Liu, K. and Zhou, Y. Effects of crustal thickness variations on surface wave phase delays. *Geophysical Journal International*, 192(2):773–792, Feb. 2013. doi: 10.1093/gji/ggs048.
- Liu, K. and Zhou, Y. Global Rayleigh wave phase-velocity maps from finite-frequency tomography. *Geophysical Journal International*, 205(1):51–66, Apr. 2016a. doi: 10.1093/gji/ggv555.
- Liu, K. and Zhou, Y. Travelling-wave Green tensor and near-field Rayleigh-wave sensitivity. *Geophysical Journal International*, 205(1):134–145, Apr. 2016b. doi: 10.1093/gji/ggv564.
- Lévéque, J., Debayle, E., and Maupin, V. Anisotropy in the Indian Ocean upper mantle from Rayleigh- and Love-waveform inversion. *Geophysical Journal International*, 133(3):529–540, June 1998. doi: 10.1046/j.1365-246X.1998.00504.x.
- Lévéque, J. J., Rivera, L., and Wittlinger, G. On the use of the checker-board test to assess the resolution of tomographic inversions. *Geophysical Journal International*, 115(1):313–318, Oct. 1993. doi: 10.1111/j.1365-246X.1993.tb05605.x.
- Ma, Z., Masters, G., Laske, G., and Pasyanos, M. A comprehensive dispersion model of surface wave phase and group velocity for the globe. *Geophysical Journal International*, 199(1):113–135, Oct. 2014. doi: 10.1093/gji/ggu246.
- Mag, A. M., Zaroli, C., and Koelemeijer, P. Bridging the gap between SOLA and deterministic linear inferences in the context of seismic tomography. *Geophysical Journal International*, 242(1), May 2025. doi: 10.1093/gji/ggaf131.
- Maggi, A., Debayle, E., Priestley, K., and Barruol, G. Azimuthal anisotropy of the Pacific region. *Earth and Planetary Science Letters*, 250(1-2):53–71, Oct. 2006a. doi: 10.1016/j.epsl.2006.07.010.
- Maggi, A., Debayle, E., Priestley, K., and Barruol, G. Multimode surface waveform tomography of the Pacific Ocean: a closer look at the lithospheric cooling signature. *Geophysical Journal International*, 166(3):1384–1397, Sept. 2006b. doi: 10.1111/j.1365-246X.2006.03037.x.
- Magrini, F., Diaferia, G., El-Sharkawy, A., Cammarano, F., van der Meijde, M., Meier, T., and Boschi, L. Surface-Wave Tomography of the Central-Western Mediterranean: New Insights Into the Liguro-Provençal and Tyrrhenian Basins. *Journal of Geophysical Research: Solid Earth*, 127(3), Mar. 2022. doi: 10.1029/2021JB023267.
- Marignier, A., Ferreira, A. M. G., and Kitching, T. The Probability of Mantle Plumes in Global Tomographic Models. *Geochemistry, Geophysics, Geosystems*, 21(9), Sept. 2020. doi: 10.1029/2020GC009276.
- Marone, F. and Romanowicz, B. Non-linear crustal corrections in high-resolution regional waveform seismic tomography. *Geophysical Journal International*, 170:460–467, Feb. 2007. doi: 10.1111/j.1365-246X.2007.03399.x.
- Marquering, H., Nolet, G., and Dahlen, F. Three-dimensional waveform sensitivity kernels. *Geophysical Journal International*, 132(3):521–534, Mar. 1998. doi: 10.1046/j.1365-246X.1998.00426.x.
- Masters, G., Woodhouse, J. H., and Freeman, G. Mineos v1.0.2, 2011. <https://geodynamics.org/cig,2011>.
- Menke, W. *Geophysical Data Analysis: Discrete Inverse Theory*. Academic Press, 1989.
- Montagner, J.-P. Upper mantle low anisotropy channels below the Pacific Plate. *Earth and Planetary Science Letters*, 202(2):263–274, Sept. 2002. doi: 10.1016/S0012-821X(02)00791-4.
- Monteiller, V., Chevrot, S., Komatitsch, D., and Wang, Y. Three-dimensional full waveform inversion of short-period teleseismic wavefields based upon the SEM–DSM hybrid method. *Geophysical Journal International*, 202(2):811–827, Aug. 2015. doi: 10.1093/gji/ggv189.
- Moulik, P., Lekic, V., Romanowicz, B., Ma, Z., Schaeffer, A., Ho, T., Beucier, E., Debayle, E., Deuss, A., Durand, S., Ekström, G., Lebedev, S., Masters, G., Priestley, K., Ritsema, J., Sigloch, K., Trampert, J., and Dziewonski, A. M. Global reference seismological data sets: multimode surface wave dispersion. *Geophysical Journal International*, 228(3):1808–1849, Dec. 2021. doi: 10.1093/gji/ggab418.
- Nolet, G. Solving or resolving inadequate and noisy tomographic systems. *Journal of Computational Physics*, 61(3):463–482, Dec. 1985. doi: 10.1016/0021-9991(85)90075-0.
- Nolet, G. *A Breviary of Seismic Tomography: Imaging the Interior of the Earth and Sun*. Cambridge University Press, 1 edition, Sept. 2008. doi: 10.1017/CBO9780511984709.
- Nolet, G., Montelli, R., and Virieux, J. Explicit, approximate expressions for the resolution and *a posteriori* covariance of massive tomographic systems. *Geophysical Journal International*, 138(1):36–44, July 1999. doi: 10.1046/j.1365-246X.1999.00858.x.
- Ouattara, Y., Zigone, D., and Maggi, A. Rayleigh wave group velocity dispersion tomography of West Africa using regional earthquakes and ambient seismic noise. *Journal of Seismology*, 23(6):1201–1221, Nov. 2019. doi: 10.1007/s10950-019-09860-z.
- Paige, C. C. and Saunders, M. A. LSQR: An Algorithm for Sparse Linear Equations and Sparse Least Squares. *ACM Transactions on Mathematical Software (TOMS)*, 8(1):43–71, Mar. 1982. doi: 10.1145/355984.355989.
- Panning, M. P., Lekić, V., and Romanowicz, B. A. Importance of crustal corrections in the development of a new global model of radial anisotropy. *Journal of Geophysical Research*, 115(B12):B12325, Dec. 2010. doi: 10.1029/2010JB007520.
- Parisi, L., Ferreira, A. M. G., and Capdeville, Y. Validity domain of the Born approximation for seismic waveform modelling in realistic 3-D Earth structure. *Geophysical Journal International*, 200(2):910–916, Feb. 2015. doi: 10.1093/gji/ggu446.
- Park, J., Lindberg, C. R., and Vernon, F. L. Multitaper spectral analysis of high-frequency seismograms. *Journal of Geophysical Research*, 92(B12):12675, 1987a. doi: 10.1029/JB092iB12p12675.
- Park, J., Vernon, F. L., and Lindberg, C. R. Frequency de-

- pendent polarization analysis of high-frequency seismograms. *Journal of Geophysical Research*, 92(B12):12664, 1987b. doi: 10.1029/JB092iB12p12664.
- Parker, R. L. Understanding Inverse Theory. *Annual Review of Earth and Planetary Sciences*, 5(1):35–64, May 1977. doi: 10.1146/annurev.ea.05.050177.000343.
- Percival, D. B. and Walden, A. T. *Spectral Analysis for Physical Applications*. Cambridge University Press, 1 edition, June 1993. doi: 10.1017/CBO9780511622762.
- Pijpers, F. P. and Thompson, M. J. Faster formulations of the optimally localized averages method for helioseismic inversions. *Astronomy and Astrophysics*, 262:L33–L36, Sept. 1992. <https://ui.adsabs.harvard.edu/abs/1992A&A...262L..33P>.
- Pijpers, F. P. and Thompson, M. J. The SOLA method for helioseismic inversion. *Astronomy and Astrophysics*, 281: 231–240, Jan. 1994. <https://ui.adsabs.harvard.edu/abs/1994A&A...281..231P>.
- Priestley, K. Seismic evidence for a moderately thick lithosphere beneath the Siberian Platform. *Geophysical Research Letters*, 30(3):1118, 2003. doi: 10.1029/2002GL015931.
- Priestley, K. and McKenzie, D. The thermal structure of the lithosphere from shear wave velocities. *Earth and Planetary Science Letters*, 244(1-2):285–301, Apr. 2006. doi: 10.1016/j.epsl.2006.01.008.
- Rawlinson, N. and Spakman, W. On the use of sensitivity tests in seismic tomography. *Geophysical Journal International*, 205(2): 1221–1243, May 2016. doi: 10.1093/gji/ggw084.
- Rawlinson, N., Fichtner, A., Sambridge, M., and Young, M. Seismic Tomography and the Assessment of Uncertainty. *Advances in Geophysics*, 55:1–76, 2014. doi: 10.1016/bs.agph.2014.08.001.
- Restelli, F., Zaroli, C., and Koelemeijer, P. Robust estimates of the ratio between S- and P-wave velocity anomalies in the Earth's mantle using normal modes. *Physics of the Earth and Planetary Interiors*, 347:107135, Feb. 2024. doi: 10.1016/j.pepi.2023.107135.
- Ritsema, J., van Heijst, H. J., and Woodhouse, J. H. Global transition zone tomography: GLOBAL TRANSITION ZONE TOMOGRAPHY. *Journal of Geophysical Research: Solid Earth*, 109(B2), Feb. 2004. doi: 10.1029/2003JB002610.
- Ritsema, J., McNamara, A. K., and Bull, A. L. Tomographic filtering of geodynamic models: Implications for model interpretation and large-scale mantle structure. *Journal of Geophysical Research*, 112(B01303), Jan. 2007. doi: 10.1029/2006JB004566.
- Ritzwoller, M. H., Shapiro, N. M., and Zhong, S.-J. Cooling history of the Pacific lithosphere. *Earth and Planetary Science Letters*, 226(1-2):69–84, Sept. 2004. doi: 10.1016/j.epsl.2004.07.032.
- Rodgers, A. J., Doody, C. D., and Fichtner, A. WUS324: Multi-scale Full Waveform Inversion Approaching Convergence Improves Waveform Fits While Imaging Seismic Structure of the Western United States. *Geophysical Research Letters*, 51(20): e2024GL110911, Oct. 2024. doi: 10.1029/2024GL110911.
- Ruan, Y. and Zhou, Y. The effects of 3-D anelasticity ( $Q$ ) structure on surface wave phase delays. *Geophysical Journal International*, 181(1):479–492, Apr. 2010. doi: 10.1111/j.1365-246X.2010.04514.x.
- Sambridge, M., Bodin, T., Gallagher, K., and Tkalčić, H. Transdimensional inference in the geosciences. *Philosophical Transactions of the Royal Society A: Mathematical, Physical and Engineering Sciences*, 371(1984):20110547, Feb. 2013. doi: 10.1098/rsta.2011.0547.
- Scales, J. A. and Snieder, R. To Bayes or not to Bayes? *GEOPHYSICS*, 62(4):1045–1046, July 1997. doi: 10.1190/1.6241045.1.
- Schuberth, B. S. A., Bunge, H., and Ritsema, J. Tomographic filtering of high-resolution mantle circulation models: Can seismic heterogeneity be explained by temperature alone? *Geochemistry, Geophysics, Geosystems*, 10(5):2009GC002401, May 2009. doi: 10.1029/2009GC002401.
- Seredkina, A. I. Surface Wave Tomography of the Arctic from Rayleigh and Love Wave Group Velocity Dispersion Data. *Izvestiya, Physics of the Solid Earth*, 55(3):439–450, May 2019. doi: 10.1134/S106935131903008X.
- Shapiro, N. M., Campillo, M., Stehly, L., and Ritzwoller, M. H. High-Resolution Surface-Wave Tomography from Ambient Seismic Noise. *Science*, 307(5715):1615–1618, Mar. 2005. doi: 10.1126/science.1108339.
- Simmons, N. A., Schuberth, B. S. A., Myers, S. C., and Knapp, D. R. Resolution and Covariance of the LLNL-G3D-JPS Global Seismic Tomography Model: Applications to Travel time Uncertainty and Tomographic Filtering of Geodynamic Models. *Geophysical Journal International*, 217(3):1543–1557, June 2019. doi: 10.1093/gji/ggz102.
- Simons, F. J., van der Hilst, R. D., Montagner, J.-P., and Zielhuis, A. Multimode Rayleigh wave inversion for heterogeneity and azimuthal anisotropy of the Australian upper mantle. *Geophysical Journal International*, 151(3):738–754, Dec. 2002. doi: 10.1046/j.1365-246X.2002.01787.x.
- Slepian, D. Prolate Spheroidal Wave Functions, Fourier Analysis, and Uncertainty-V: The Discrete Case. *Bell System Technical Journal*, 57(5):1371–1430, May 1978. doi: 10.1002/j.1538-7305.1978.tb02104.x.
- Snieder, R. 3-D linearized scattering of surface waves and a formalism for surface wave holography. *Geophysical Journal International*, 84(3):581–605, Mar. 1986. doi: 10.1111/j.1365-246X.1986.tb04372.x.
- Snieder, R. An extension of Backus-Gilbert theory to nonlinear inverse problems. *Inverse Problems*, 7(3):409–433, June 1991. doi: 10.1088/0266-5611/7/3/008.
- Snieder, R. and Nolet, G. Linearized scattering of surface waves on a spherical Earth. *Journal of Geophysics*, 61(1):55–63, 1987.
- Socco, L. V., Foti, S., Comina, C., and Boiero, D. Comment on 'Shear wave profiles from surface wave inversion: the impact of uncertainty on seismic site response analysis'. *Journal of Geophysics and Engineering*, 9(2):241–243, Apr. 2012. doi: 10.1088/1742-2132/9/2/241.
- Tarantola, A. *Inverse Problem Theory and Methods for Model Parameter Estimation*. Society for Industrial and Applied Mathematics, Jan. 2005. doi: 10.1137/1.9780898717921.
- Tarantola, A. and Valette, B. Generalized nonlinear inverse problems solved using the least squares criterion. *Reviews of Geophysics*, 20(2):219, 1982. doi: 10.1029/RG020i002p00219.
- Thomson, D. Spectrum estimation and harmonic analysis. *Proceedings of the IEEE*, 70(9):1055–1096, 1982. doi: 10.1109/PROC.1982.12433.
- Thrustarson, S., Van Herwaarden, D.-P., Noe, S., Josef Schiller, C., and Fichtner, A. REVEAL: A Global Full-Waveform Inversion Model. *Bulletin of the Seismological Society of America*, 114(3): 1392–1406, June 2024. doi: 10.1785/0120230273.
- Tian, Y., Zhou, Y., Sigloch, K., Nolet, G., and Laske, G. Structure of North American mantle constrained by simultaneous inversion of multiple-frequency SH, SS, and Love waves. *Journal of Geophysical Research*, 116(B2):B02307, Feb. 2011. doi: 10.1029/2010JB007704.
- Trampert, J. Global seismic tomography: the inverse problem and beyond. *Inverse Problems*, 14(3):371–385, June 1998. doi: 10.1088/0266-5611/14/3/002.
- Tromp, J., Komatitsch, D., Hjörleifsdóttir, V., Liu, Q., Zhu, H., Peter,



- D., Bozdog, E., McRitchie, D., Friberg, P., Trabant, C., and Hutko, A. Near real-time simulations of global CMT earthquakes: Near real-time simulations of CMT earthquakes. *Geophysical Journal International*, 183(1):381–389, Oct. 2010. doi: 10.1111/j.1365-246X.2010.04734.x.
- Wiggins, R. A. The general linear inverse problem: Implication of surface waves and free oscillations for Earth structure. *Reviews of Geophysics*, 10(1):251, 1972. doi: 10.1029/RG010i001p00251.
- Yomogida, K. Fresnel zone inversion for lateral heterogeneities in the earth. *pure and applied geophysics*, 138(3):391–406, Sept. 1992. doi: 10.1007/BF00876879.
- Yoshizawa, K. and Kennett, B. L. N. Multimode surface wave tomography for the Australian region using a three-stage approach incorporating finite frequency effects: THREE-STAGE SURFACE WAVE TOMOGRAPHY. *Journal of Geophysical Research: Solid Earth*, 109(B2), Feb. 2004. doi: 10.1029/2002JB002254.
- Yoshizawa, K. and Kennett, B. L. N. Sensitivity kernels for finite-frequency surface waves. *Geophysical Journal International*, 162(3):910–926, Sept. 2005. doi: 10.1111/j.1365-246X.2005.02707.x.
- Zaroli, C. Global seismic tomography using Backus-Gilbert inversion. *Geophysical Journal International*, 207(2):876–888, Nov. 2016. doi: 10.1093/gji/ggw315.
- Zaroli, C. Seismic tomography using parameter-free Backus-Gilbert inversion. *Geophysical Journal International*, 218(1): 619–630, July 2019. doi: 10.1093/gji/ggz175.
- Zaroli, C., Koelemeijer, P., and Lambotte, S. Toward Seeing the Earth's Interior Through Unbiased Tomographic Lenses. *Geophysical Research Letters*, 44(22):11,399–11,408, Nov. 2017. doi: 10.1002/2017GL074996.
- Zhang, X., Curtis, A., Galetti, E., and de Ridder, S. 3-D Monte Carlo surface wave tomography. *Geophysical Journal International*, 215(3):1644–1658, Dec. 2018. doi: 10.1093/gji/ggy362.
- Zhang, X., Roy, C., Curtis, A., Nowacki, A., and Baptie, B. Imaging the subsurface using induced seismicity and ambient noise: 3-D tomographic Monte Carlo joint inversion of earthquake body wave traveltimes and surface wave dispersion. *Geophysical Journal International*, 222(3):1639–1655, Sept. 2020. doi: 10.1093/gji/ggaa230.
- Zhou, Y. Multimode surface wave sensitivity kernels in radially anisotropic earth media. *Geophysical Journal International*, 176(3):865–888, Mar. 2009a. doi: 10.1111/j.1365-246X.2008.04010.x.
- Zhou, Y. Surface-wave sensitivity to 3-D anelasticity. *Geophysical Journal International*, 178(3):1403–1410, Sept. 2009b. doi: 10.1111/j.1365-246X.2009.04230.x.
- Zhou, Y., Dahlen, F. A., and Nolet, G. Three-dimensional sensitivity kernels for surface wave observables. *Geophysical Journal International*, 158(1):142–168, July 2004. doi: 10.1111/j.1365-246X.2004.02324.x.
- Zhou, Y., Dahlen, F. A., Nolet, G., and Laske, G. Finite-frequency effects in global surface-wave tomography. *Geophysical Journal International*, 163(3):1087–1111, Dec. 2005. doi: 10.1111/j.1365-246X.2005.02780.x.
- Zhou, Y., Nolet, G., Dahlen, F. A., and Laske, G. Global upper-mantle structure from finite-frequency surface-wave tomography. *Journal of Geophysical Research*, 111(B04304), 2006. doi: 10.1029/2005JB003677.

## Appendix A: The SOLA method in more detail

In this appendix, we provide more details on the SOLA method inspired by Zaroli (2016); Zaroli et al. (2017); Zaroli (2019). Here we use a slightly different notation following Lattalier et al. (2022). Let us consider  $N$  data that are gathered in a data vector  $\mathbf{d} \in \mathcal{R}^N$ . In addition, the continuous ‘true’ model is discretised with model parameters gathered in a model vector  $\mathbf{m} \in \mathcal{R}^M$ . Assuming linearity, the data are expressed as linear combination of the model parameters  $\mathbf{d} = \mathbf{G}\mathbf{m}$ , where the forward mapping  $\mathbf{G} \in \mathcal{R}^{N \times M}$  contains the physical laws relating the  $N$  data to the  $M$  model parameters. This forward mapping includes theoretical errors as  $\mathbf{G}$  does not exactly predict what we aim to measure. Additionally, the measurement introduces data errors (the measurement does not exactly measure what we aim to measure). We first discuss SOLA without theoretical and measurement errors and come back to these later on.

The inverse problem is ill-posed, i.e.  $\mathbf{G}$  is not invertible and we cannot find a unique value for each model parameter. With SOLA, we break this non-uniqueness by instead finding a single value for a local average (Zaroli, 2016). Here, we define this local average as a combination of model parameters that is informative, i.e. a weighted sum of model parameters that is local to a model parameter location. The weights of such a sum is the resolution of the specific model parameter.

Let  $\tilde{\mathbf{m}}^{(k)} \in \mathcal{R}$  be the estimate of a local average around model parameter  $k$  and let us write this estimate as a linear combination of the data  $\tilde{\mathbf{m}}^{(k)} = \mathbf{G}^{\dagger(k)} \mathbf{d}$ , where  $\mathbf{G}^{\dagger(k)} \in \mathcal{R}^N$  is the vector containing the weights for the linear combination of the data. We use the forward equation to obtain  $\tilde{\mathbf{m}}^{(k)} = \mathbf{G}^{\dagger(k)} \mathbf{G} \mathbf{m}$ , which implies that the vector  $\mathbf{G}^{\dagger(k)} \mathbf{G}$  contains the weights specifically for the local average of model parameter  $k$ . This defines the resolution for this model parameter:  $\mathbf{R}^{(k)} = (\mathbf{R}_j^{(k)})_{j=1,\dots,M} = (\sum_{i=1}^N \mathbf{G}_i^{\dagger(k)} \mathbf{G}_{ij})_{j=1,\dots,M}$ . To account for varying voxel volumes, we define the averaging kernel  $\mathbf{A}^{(k)} = (\mathbf{A}_j^{(k)})_{j=1,\dots,M} = (\mathbf{R}_j^{(k)} / V_j)_{j=1,\dots,M}$ . To find  $\mathbf{G}^{\dagger(k)}$  we design a target local average, or target kernel,  $\mathbf{T}^{(k)} \in \mathcal{R}^M$  and minimise the squared distance between the averaging and target kernel:

$$\mathbf{G}^{\dagger(k)} = \arg \min_{\mathbf{G}^{\dagger(k)}} \sum_{j=1,\dots,M} V_j \left[ \left( \sum_{i=1,\dots,N} \mathbf{G}_i^{\dagger(k)} \mathbf{G}_{ij} / V_j \right) - \mathbf{T}_j^{(k)} \right]^2 \quad (10)$$

The aim of the minimisation problem in Equation 10 is to fit the target kernel given the limits imposed by the data sensitivity, i.e. the geometry of the problem. In addition, we can add a uni-modularity constraint on the resolution for the local average to be unbiased:  $\sum_{ij} \mathbf{G}_i^{\dagger(k)} \mathbf{G}_{ij} = 1$  (Zaroli et al., 2017). Values greater or smaller than unity imply that the local average is artificially over- or under-estimating the average of the ‘true’ model parameter. Note that if we compute the linear combination  $\mathbf{G}^{\dagger(k)}$  for all  $M$  model parameters, and organise them into a matrix  $\mathbf{G}^{\dagger}$ , then we can write

$\tilde{m} = G^\dagger d$  and  $\tilde{m} = G^\dagger Gm$ , where  $\tilde{m} \in \mathcal{R}^M$  is the collection of local average estimates. In fact,  $G^\dagger$  is the generalised inverse for the inverse problem, and  $\tilde{m}$  is the model solution. This model solution can be visualised, as we have done in this study, but it is important to recall that this model solution is nothing more than a collection of local averages, not estimates of individual model parameters.

The above is incomplete as all observed data contain errors. To account for this, we can represent each datum as a Gaussian probability distribution whose mean is the measured datum ( $d_i$ ) and whose standard deviation is the estimated measurement uncertainty ( $\sigma_{d_i}$ ). Under this assumption, a model parameter estimate is also a Gaussian probability distribution as it is a linear combination of Gaussian probability distributions and we can easily compute its mean and standard deviation. The mean of the local average distribution is still given by  $\tilde{m}^{(k)} = \sum_{i=1}^N G_i^{\dagger(k)} d_i$ , while the standard deviation is given by  $\sigma_{\tilde{m}^{(k)}} = \sqrt{\sum_{i=1}^N G_i^{\dagger(k)2} \sigma_{d_i}^2}$ . Note that the model uncertainty is for a local average estimate, not an estimate for a given model parameter. The weights that specify the linear combination of data ( $G_i^{\dagger(k)}$ ) also influence the propagation of data uncertainty into model uncertainty. To account for this in designing  $G^{\dagger(k)}$ , i.e. to find a combination of model parameters that also minimises the propagation of data uncertainty into model uncertainty, we amend the minimisation problem of Equation 10:

$$G^{\dagger(k)} = \arg \min_{G^{\dagger(k)}} \sum_{j=1, \dots, M} V_j \left[ \left( \sum_{i=1, \dots, N} G_i^{\dagger(k)} G_{ij} / V_j \right) - T_j^{(k)} \right]^2 + \eta^k \left( \sum_{i=1, \dots, N} G_i^{\dagger(k)2} \sigma_{d_i}^2 \right) \quad (11)$$

$$\text{s.t. } \sum_{ij} G_i^{\dagger(k)} G_{ij} = 1.$$

with  $\eta^k$  the trade-off parameter for the model parameter. Equation 11 leads to a set of equations for each model parameter  $k$  with its particular target resolution  $T^{(k)}$ . These can be solved, as proposed by Zaroли (2016), using an LSQR algorithm (e.g. Paige and Saunders, 1982). More details on this implementation can be found in appendix A1 of Zaroли (2016). A summary of the SOLA inversion illustrating the inputs and outputs is presented in Figure 10.

## Appendix B: Phase delay measurements using multi-taper technique

Let  $s(\omega) = A(\omega)e^{\phi(\omega)}$  be the mathematical expression of the reference seismogram computed for the 1D reference model for a given source-receiver pair at some frequency  $\omega$ , with amplitude  $A$  and phase  $\phi$ . Let  $o(\omega) =$

$A^o(\omega)e^{\phi^o(\omega)}$  be defined equivalently for the observed seismogram, or the SEM seismogram in the case of this synthetic study. The accumulated phase results from source and receiver effects, caustics and the propagation itself (e.g. Ekström, 2011; Ma et al., 2014; Moulik et al., 2021). We typically assume the first three terms are the same for both the reference and observed seismograms. In that case, the phase delay can be directly related to the propagation and thus perturbations in the Earth model. These phase delays are what we are interested in measuring here.

An overview of the measurement workflow is given schematically in Figure 11. Waveforms are first pre-processed (e.g. resampled at 1 Hz, instrumental response removed if necessary). As suggested by Zhou et al. (2005) and Zhou (2009a), we then use a multi-taper technique to measure the phase-delays and to obtain an estimate of the measurement uncertainty (e.g. Thomson, 1982; Park et al., 1987a,b; Laske et al., 1994; Laske and Masters, 1996; Hjörleifsdóttir, 2007). The technique uses the first few Slepian functions (after Slepian, 1978) defined over a 801 s window. Slepian functions are an infinite series of functions with optimal frequency spectrum (therefore reducing frequency leakage) that weigh different parts of the waveform (thus reducing bias in the time-domain). With a 801 s-long time-window and 1 Hz sampling rate, we should use only the first 5 Slepian functions (see Percival and Walden, 1993, pp. 331). To position the Slepian functions, we compute the predicted group arrival time at the frequency of interest, starting the Slepian time window 150 s before the expected arrival. We then apply a 4 mHz-wide bandpass filter around the frequency of interest before we compute the Fast Fourier Transform. Finally, we subtract the phase component of the tapered and filtered observed (or SEM here) waveform from the reference waveform in the frequency domain. Usually, we obtain a smooth dispersion curve, except for when the phase delay reaches  $\pm\pi$ , where the dispersion curve makes jumps of  $\pm 2\pi$ . Low frequencies are less likely to suffer from cycle-skips. Therefore, we make our measurements at increasingly higher frequency, starting at 6 mHz. When we detect these so-called cycle-skips (we use a threshold of  $\pm 4$  radians for the detection), we add or remove  $2\pi$  to obtain a smooth dispersion curve and apply this correction accordingly to all higher frequencies.

For each source-receiver pair, we end up with 5 dispersion curves for the 5 Slepian functions, corrected for cycle-skipping. We use the average of these 5 curves as our final measurements and the standard deviation as the data measurement uncertainty. In some cases, we note an inaccurate detection of cycle-skipping (either as false-positive or false-negative). These false detections typically do not occur on all five tapers, leading to a sharp increase in measurement uncertainty. In addition, some fundamental mode measurements are contaminated by the interference of other phases or higher modes. This usually does not affect all five tapers, thus also leading to an increase in the measurement uncertainty.

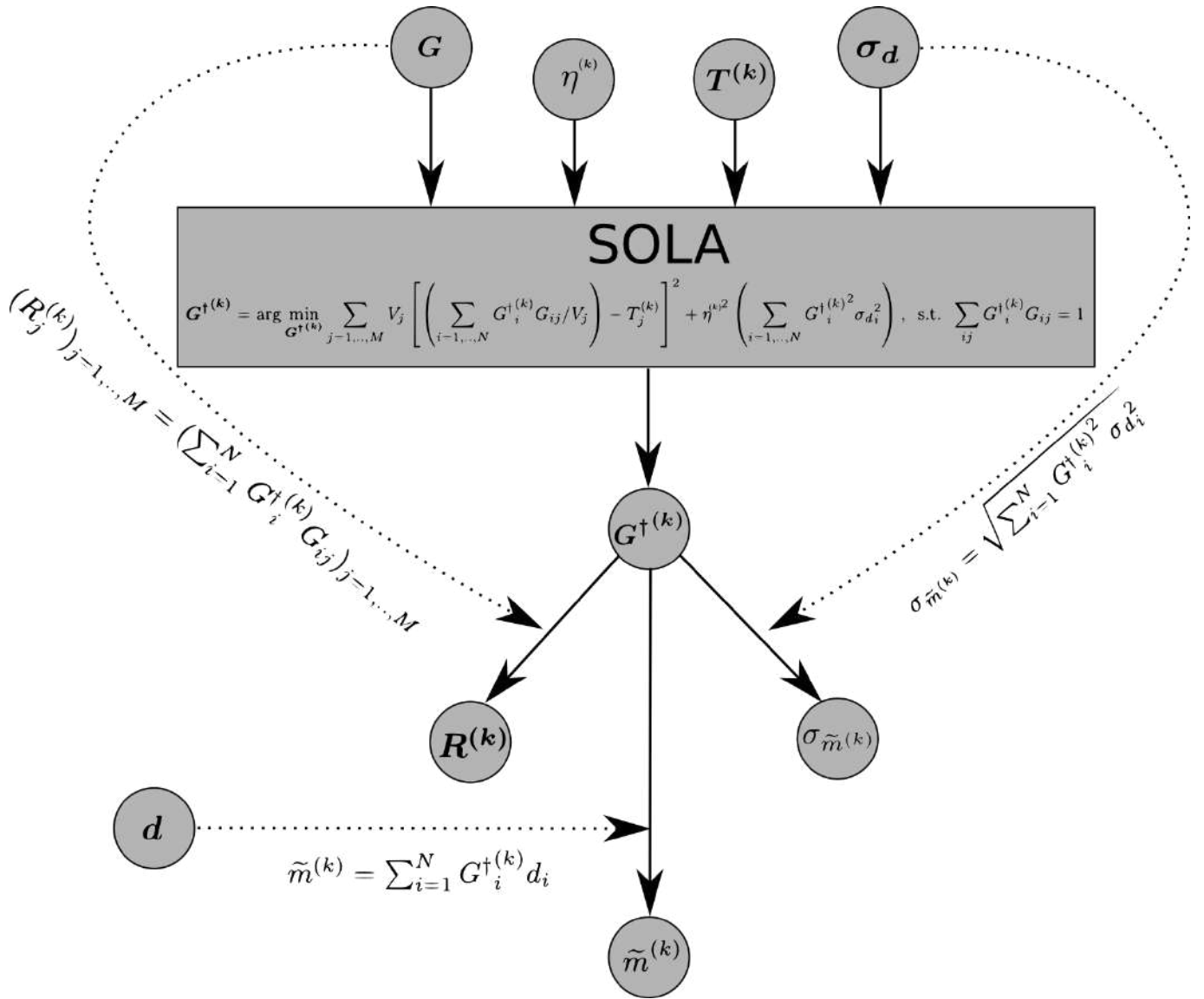


**Figure 10** Illustration of the SOLA workflow. The minimisation problem at the heart of SOLA aims to find a generalised inverse matrix  $\mathbf{G}^{\dagger(k)}$  such that the resolution is close to the target resolution and that the model uncertainty  $\sigma_{\tilde{m}^{(k)}}$  is reasonable. This minimisation problem takes four inputs:  $G$ ,  $\eta^k$ ,  $\sigma_d$  and  $T^{(k)}$ . The sensitivity matrix  $G$  contains the forward theory and depends on the data geometry. The measurement uncertainties  $\sigma_d$  are estimated using the multitaper technique. For model parameter  $k$ , a target resolution is designed  $T^{(k)}$  and a trade-off parameter  $\eta^k$  balancing the fit to the target resolution and model uncertainty is chosen. The obtained generalised inverse allows us to compute the model uncertainty  $\sigma_{\tilde{m}^{(k)}}$  using the data uncertainty, to compute the averaging kernel  $\mathbf{R}^{(k)}$  by combining the generalised inverse with the sensitivity matrix  $G$ , and to compute the model parameter estimate  $\tilde{m}^{(k)}$  from the data values  $d$ . Note that the data values only play a role after the minimisation problem and that no *a priori* on the model estimate itself has been introduced. In this study, we set the measurement uncertainty to 1 as input into the SOLA minimisation problem. However, we incorporate the actual measurement uncertainty to compute the measurement model uncertainty.



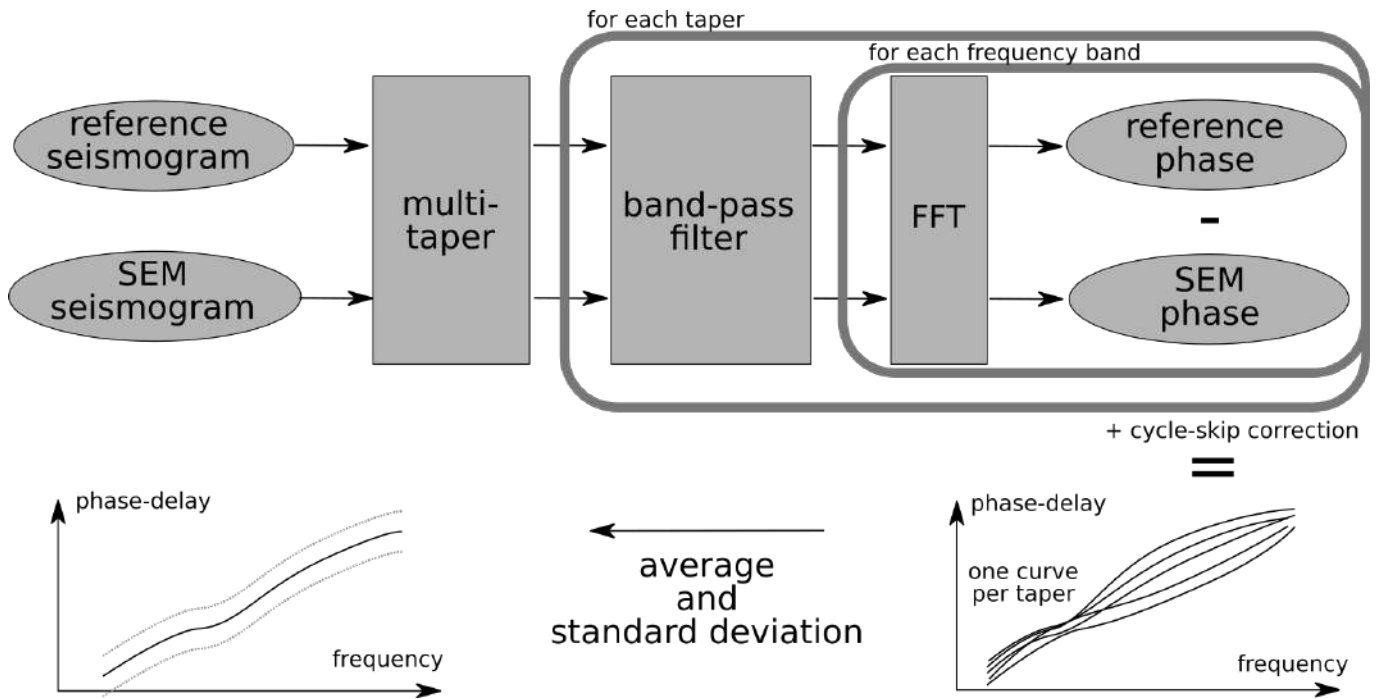


**Figure 11** Overview of the measurement workflow. We compute a reference seismogram for the reference radial Earth model, which we use to measure the phase-delay of a SEM-computed seismogram (acting in this synthetic setup as observed seismogram). We apply a set of tapers (the five first Slepians), thus leading to 5 tapered traces. We filter each in a set of frequency bands, before we take the FFT. In the frequency domain, we then compute the phase difference for all frequencies for all tapers, producing a set of 5 dispersion curves. We apply a cycle-skip correction and then take the mean of all 5 tapers as the final measurement, with the measurement uncertainty given by the standard deviation of the five tapers.

## Appendix C: Computational considerations

In this study, we use  $N = 47\,700$  fundamental mode phase delays as data and we parameterise the spatial domain into  $M = 259\,200$  voxels (cells of size  $2^\circ \times 2^\circ$  laterally and 25 km depth for the first 400 km depth of the whole mantle). Therefore, the sensitivity matrix  $G$  of size  $N \times M$  is reasonably large. To optimise the sparsity of the sensitivity matrix, we only consider the sensitivity kernels in the two first Fresnel zones laterally, since their amplitude is negligible further away. The sensitivity is also negligible at depths greater than 400 km depth. Our resulting matrix thus contains 645 282 622 non-zero elements, i.e. the density is approximately 5.2%. The SOLA optimisation problem (Equation 5) leads to a set of normal equations taking the form of another  $(M + 1) \times (N - 1)$  matrix  $Q$  that is less sparse than  $G$  (see Zaroli, 2016, Appendix A1). Reordering the lines of  $G$  with the sparsest row first helps to improve the sparsity of  $Q$ . In this study,  $Q$  contains 657 124 288 non-zero elements, i.e. sparsity is approximately 5.3%. On disk, we use a ‘coordinate list’ (COO) storage strategy, and  $Q$  takes up  $\sim 17$  GB. On RAM, we use a reversed linked-chain storage strategy to improve compute time. In this case, the  $Q$  matrix takes up  $\sim 35$  GB. This large memory requirement is the primary limiting factor for increasing the number of data and model parameters.

The computation time of the LSQR inversion for a single model parameter depends on the target resolution and trade-off parameter. With the choices made in this study, it takes  $\sim 100$  s per model parameter. As we invert

for 69 200 model parameters, a full model estimate thus requires  $\sim 692\,000$  s CPU time (or 192 CPUh). In practice, we invert for model parameters in parallel on several nodes with 128 CPU each using a multi-threading approach with OpenMP. The scaling is not fully linear due to input/output operations, but this strategy reduces the wall time to  $\sim 20$  h.

The article *Towards surface-wave tomography with 3D resolution and uncertainty* © 2025 by Franck Latallier is licensed under CC BY 4.0.